Convective Momentum Transport Associated with the Madden–Julian Oscillation Based on a Reanalysis Dataset

JI-HYUN OH, XIANAN JIANG, AND DUANE E. WALISER

Joint Institute for Regional Earth System and Engineering, University of California, Los Angeles, Los Angeles, and Jet Propulsion Laboratory, California Institute of Technology, Pasadena, California

MITCHELL W. MONCRIEFF

National Center for Atmospheric Research, Boulder, Colorado*

RICHARD H. JOHNSON

Colorado State University, Fort Collins, Colorado

(Manuscript received 13 August 2014, in final form 31 March 2015)

ABSTRACT

A better understanding of multiscale interactions within the Madden–Julian oscillation (MJO), including momentum exchanges, is critical for improved MJO prediction skill. In this study, convective momentum transport (CMT) associated with the MJO is analyzed based on the NOAA Climate Forecast System Reanalysis (CFSR). A three-layer vertical structure associated with the MJO, as previously suggested in the mesoscale momentum tendency profile based on global cloud-resolving model simulations, is evident in the subgrid-scale momentum tendency from the CFSR. Positive (negative) subgrid-scale momentum tendency anomalies are found near the surface, negative (positive) anomalies are found in the low to midtroposphere, and positive (negative) anomalies in the upper troposphere are found within and to the west (east) of the MJO convection. This tends to damp the MJO circulation in the free atmosphere, while enhancing MJO winds near the surface. In addition, it could also reduce the MJO eastward propagation speed and lead to the backward tilt with height in the observed MJO structure through a secondary circulation near the MJO center. Further analyses illustrate that this three-layer vertical structure in subgrid-scale momentum tendency largely balances the grid-scale momentum transport of the zonal wind component u, mainly through the transport of seasonal mean u by the MJO-scale vertical motion. Synoptic-scale systems, which were previously proposed to be essential for the u-momentum transport of the MJO, however, are found to play a minor role for the total grid-scale momentum tendency. The above momentum tendency structure is also confirmed with the ECMWF analysis for the Year of Tropical Convection (YOTC) that lends confidence to these above results based on the CFSR.

1. Introduction

As one of the most pronounced modes of tropical climate variability, the Madden–Julian oscillation (MJO; Madden and Julian 1971, 1994) plays a critical role in bridging global weather and climate and serves as one of the primary predictability sources for extended-range forecasts (Lau and Waliser 2012; Zhang 2005). The MJO is often initiated over the western equatorial Indian Ocean (IO) and propagates eastward along the equator at a phase speed of about 5 m s^{-1}. Exhibiting a planetary spatial scale of about 5000–10 000 km, the MJO is characterized by organization of a hierarchy of multiscale convective systems (MCSs; Moncrieff et al. 2012). The slow eastward-migrating MJO envelope contains embedded fast eastward-moving super cloud clusters (SCC) with horizontal scales of a several thousand kilometers that, in turn, is composed of smaller westward-moving cloud clusters (Nakazawa 1988; Takayabu 1994; Roundy 2008; Kiladis et al. 2009). The SCCs have been identified

* The National Center for Atmospheric Research is sponsored by the National Science Foundation.

Corresponding author address: Dr. Xianan Jiang, Jet Propulsion Laboratory, California Institute of Technology, MS 233-300, 4800 Oak Grove Drive, Pasadena, CA 91109.
E-mail: xianan@ucla.edu

DOI: 10.1175/JCLI-D-14-00570.1

as convectively coupled Kelvin waves (Nakazawa 1988; Takayabu and Murakami 1991; Takaya and Nakamura 2001), and the westward-moving cloud clusters as westward inertia–gravity waves, or so-called 2-day waves (Chen et al. 1996; Takayabu et al. 1996). These convectively coupled waves (CCWs) further consist of scattered cumulus clouds and organized mesoscale convective systems or squall lines.

In spite of the recent great efforts toward improving the ability of general circulation models (GCMs) to simulate the MJO, significant challenges still remain for current GCMs to produce more-realistic MJO simulations (Slingo et al. 1996; Lin et al. 2006; Kim et al. 2009; Hung et al. 2013; Jiang et al. 2015). There is a general consensus that large deficiencies in current GCMs in representing the MJO could be primarily due to our lack of understanding the interactions between the MJO and embedded multiscale convective systems (e.g., Majda 2007; Moncrieff 2010; Moncrieff et al. 2012; Zhang et al. 2013). The importance of depicting the multiscale convection organization of the MJO is further supported by the improvement of MJO simulations in recent global cloud-resolving models (Miura et al. 2007) and superparameterized GCMs (Benedict and Randall 2009). On the one hand, dynamical (e.g., vertical wind shear and convergence) and thermodynamical (moisture and instability) conditions associated with the MJO can exert significant modulations on the activity of CCWs and MCSs; on the other hand, these small-scale convective systems can feed back to the MJO through significant upscale transport of moisture, heating, and momentum (e.g., Houze 1973, 2004; Houze et al. 2000; Majda and Biello 2004; Khouider et al. 2012b; Majda and Stechmann 2015). While most previous studies have focused on collective impacts of multiscale convective systems on thermodynamic properties of the MJO, recent limited observational studies and idealized modeling work have suggested that convective momentum transport (CMT) by smaller convective systems could also play a critical role for the observed MJO structure [see recent reviews by Majda and Stechmann (2011, 2015)].

It is generally considered that unorganized cumulus convection tends to damp the large-scale flow as a frictional process. That is, it acts downscale to the environmental vertical wind shear (Majda and Stechmann 2008; Khouider et al. 2012b). In contrast, organized MCSs and CCWs can have either upgradient (amplifying) or downgradient (weakening) effects on the large-scale winds as a direct effect of the vertical tilt of the associated circulation (Moncrieff 1992; Moncrieff and Klinker 1997, hereafter MK97; Majda and Stechmann 2009). Backward vertical tilting structures of convective systems relative to their propagation direction have been widely observed (Mapes et al. 2006; Kiladis et al. 2009), with scales ranging from meso- (MCSs), to synoptic (CCWs), to planetary (MJO) scale. Moreover, GCM studies suggest that representation of mean climate (Kim et al. 2008; Richter and Rasch 2008; Song et al. 2008) as well as the MJO (Wu et al. 2007; Deng and Wu 2010; Zhou et al. 2012) is significantly improved by including the CMT effects in climate models. Thus, there has been increasing interest in exploring the CMT associated with these multiscale convective systems, particularly its role in the evolution of the MJO circulation, which is the focus of this study.

By conducting a residual budget analysis on the momentum equation, Tung and Yanai (2002a,b) analyzed the evolution of CMT profiles associated with the two major MJO events over the equatorial western Pacific (WP) during the Tropical Ocean and Global Atmosphere Coupled Ocean–Atmosphere Response Experiment (TOGA COARE; Webster and Lukas 1992). During the westerly onset phase of the MJO, it was suggested that kinetic energy is transferred upscale from subgrid-scale systems to the large-scale zonal flow, thus helping to enhance the MJO low-level westerly wind (Tung and Yanai 2002b). After the low-level westerly wind fully developed (MJO westerly wind burst phase), however, the CMT largely acts as a friction by decelerating the large-scale zonal flow and reducing the zonal wind shear. By using radar data during the same TOGA COARE period and focusing on the CMT induced by mesoscale super convective systems, Houze et al. (2000) identified strong midlevel inflow associated with mesoscale downdraft in MCSs. In the MJO westerly onset region, this mesoscale inflow transports easterly momentum downward, thus reducing the westerlies near the surface; while in the strong westerly region, the mesoscale inflow jets bring westerly momentum downward, accelerating the westerly wind burst of the MJO. These interesting observational findings motivated many follow-up investigations on the role of CMT for the MJO (e.g., Majda and Stechmann 2008, 2009; Wang and Liu 2011; Khouider et al. 2012a; Miyakawa et al. 2012), most of which were based on a simplified theoretical framework.

The multiscale organization of tropical convection is very difficult to realistically represent in current climate models because of model deficiencies in parameterizing the moist convection and insufficient horizontal resolution to adequately resolve MCSs and even CCWs. Therefore, a so-called multicloud model approach has been recently employed to study interactions between multiscale tropical convection and the large-scale environment (Khouider 2006, 2007; Khouider and Majda 2006, 2008a,b). The concept of a multicloud model is mainly based on a representation of the transition between three different cloud types—namely, congestus, deep convective, and stratiform clouds—as observed during the evolution

of tropical convection (Lin and Johnson 1996; Johnson et al. 1999; Kikuchi and Takayabu 2004; Jiang et al. 2011; Del Genio et al. 2012). A significant improvement of the MJO simulations was also achieved by implanting the multicloud model in GCMs (Khouider et al. 2011; Ajayamohan et al. 2013). Based on the multicloud model framework, Majda and Stechmann (2009) demonstrated that a two-way interaction between large-scale circulation and CCW activity can lead to an oscillation of the large-scale flow on an intraseasonal time scale. By neglecting the Coriolis force, propagation of CCWs in this model is controlled by advection of large-scale flow. Because of its westward tilt with height in the circulation, the Kelvin wave–like eastward CCWs tend to enhance lower-level large-scale westerly winds. The increased vertical zonal wind shear, however, tends to damp the eastward-propagating CCWs themselves, while favoring the westward inertial gravity (WIG)-like CCWs. As a result, the prevalence of the westward-propagating CCWs leads to the reduction of low-level westerlies and restores an environment favorable for eastward CCWs. Hence, the oscillation in the large-scale circulation continues.

This two-way interaction between the large-scale circulation and CCWs critically relies on the way that CCWs respond to changes in the environmental flow. Modulation of Kelvin and WIG-like CCWs by vertical wind shear, as illustrated by Majda and Stechmann (2009), was further confirmed by experiments based on a similar multicloud model but on a beta plane (Han and Khouider 2010; Khouider et al. 2012b). In particular, MJO modulation of convective activity was examined in detail in Khouider et al. (2012b) by specifying observed background wind shear and moisture profiles during different MJO phases in the model. It was suggested that Kelvin waves are most favored to the east of MJO convection, where strong westerly vertical wind shear (easterlies at the lower level and westerlies at the upper level) prevails, which is expected to decelerate the MJO circulation. Meanwhile, largely fed by the environmental moisture, MCSs or squall-line systems tend to be prominent in the convectively active region near the MJO center. Moving along the low-level environmental flow, the CMT induced by these organized MCSs might play a role in accelerating the MJO circulation on both sides of the MJO center, as also suggested in other studies (Majda and Stechmann 2008; Khouider et al. 2012a). To the west of the MJO center away from the core active region, picked by the strong easterly wind shear, the WIG waves are most active and tend to damp the large-scale winds.

By considering a Kelvin (WIG) wave on the west (east) side of the MJO convection, Wang and Liu (2011) examined the CMT impact from the CCWs on the instability and propagation of the MJO based on a 2.5-layer intermediate model (Wang and Li 1994). While the CMT effect itself by Kelvin and WIG waves under this configuration did not contribute to the propagation of the MJO mode in this model, inclusion of the CMT impact in addition to the frictional convective instability of the second kind (CISK) can lead to a more-realistic growth rate and propagation speed of the model MJO. This result, however, is highly sensitive to the preference of CCW activity relative to the MJO. While prescription of the WIG wave to the east of the MJO in Wang and Liu (2011) was largely motivated by the observational analysis in Kikuchi and Wang (2010) for a limited period of the summer of 1990, enhanced WIG wave activity to the east of the MJO differs from the multicloud model results mentioned above. In general, how CCW activity is modulated by the MJO in reality is not yet fully understood and has not been comprehensively characterized based on available observations.

Recently, Miyakawa et al. (2012) quantitatively analyzed CMT profiles associated with the MJO based on output from a global 7-km cloud-system-resolving model (CRM), the Nonhydrostatic Icosahedral Atmospheric Model (NICAM; Satoh et al. 2008), for a period of 32 days from 15 December 2006, which mainly covered one MJO event, as reported in Miura et al. (2007). It was illustrated that the mesoscale convection-induced CMT in the zonal wind component u exhibits the largest amplitude to the west of the MJO center, with a well-defined three-layer vertical structure: positive u-momentum tendency near the surface, negative from the lower to middle troposphere, and positive in the upper troposphere. It was proposed that this mesoscale CMT effect could be partially responsible for the vertical tilt in the observed MJO structure, delay the eastward progress of the low- to midtroposphere westerly wind, and thus reduce the MJO propagation speed.

Despite the accumulating evidence of its significant role for the MJO, as suggested by previous studies, our understanding of CMT processes remains limited. In particular, previous results in characterizing the CMT of the MJO based on the TOGA COARE field campaign and CRM simulations involve just a few MJO events with a limited focus over the WP. Additionally, although theoretical studies with simplified assumptions have provided great insight into the multiscale interactions associated with the MJO through CMT, they necessitate observational verification.

In this study, we analyze characteristics of the CMT related to the MJO over the IO and WP, mainly using a relatively long-term (12 yr) and high-resolution (50 km) state-of-the-art reanalysis dataset generated by a GCM that parameterizes the CMT as a result of subgrid-scale processes (subgrid-scale CMT). Note that the terminology of CMT in this study is intended to represent momentum transports either directly through parcel up- and downdrafts in scattered cumuli or MCSs, or eddy

momentum transports through organized circulation associated with MCSs or CCWs where a local convective signal may not be explicitly evident. This paper is structured as follows. Datasets and approaches used for the analysis are described in section 2. In section 3, detailed structures of momentum transport associated with the MJO by both subgrid- and resolved-scale processes based on the reanalyses are examined. A summary and discussion are presented in section 4.

2. Data and methods

a. Data

The dataset mainly used for this study is the Climate Forecast System Reanalysis (CFSR; data downloaded from http://nomads.ncdc.noaa.gov/modeldata/, accessed July 2013; Saha et al. 2010) from the National Centers for Environmental Prediction (NCEP). The CFSR is generated by the NCEP Global Forecast System (GFS) atmospheric model at a global horizontal resolution of spectral T382 (~38 km) with 64 native vertical levels, coupled to the Geophysical Fluid Dynamics Laboratory (GFDL) Modular Ocean Model (MOM), version 4. The GFS takes into account the CMT using a simplified Arakawa–Schubert cumulus scheme by allowing both up- and downdraft mass fluxes to transport momentum (Arakawa and Schubert 1974; Pan and Wu 1995; Moorthi et al. 2001). The CFSR dataset used for this study was archived at a 0.5° × 0.5° spatial resolution with 37 pressure levels and at a 6-hourly temporal interval.

The European Centre for Medium-Range Forecasts (ECMWF) analysis data for the 2-yr period from May 2008 to April 2010 during the Year of Tropical Convection (YOTC, hereafter referred to as the EC–YOTC dataset; Moncrieff et al. 2012; Waliser et al. 2012 data downloaded from http://apps.ecmwf.int/datasets/data/yotc-od/, accessed July 2013) were also utilized to provide an independent validation of the CMT features of the MJO as revealed in the CFSR. The EC–YOTC dataset used in this study has a 0.5° × 0.5° spatial resolution, 25 pressure levels, and a 6-hourly temporal resolution.

Additionally, 3-hourly TRMM 3B42 dataset, version 7 (data downloaded from http://disc.sci.gsfc.nasa.gov/precipitation/documentation/TRMM_README, accessed July 2013; Huffman et al. 1995), rainfall data are also employed to assess the fidelity of the CFSR to represent the MJO. The TRMM data are derived from the combination of high quality microwave estimates calibrated with infrared (IR) estimates and rain gauge analyses. The dataset covers 50°S–50°N with a 0.25° longitude–latitude spatial resolution at a 3-hourly time interval.

This study focuses on the wintertime [November–April (NDJFMA)], when the MJO exhibits its strongest variability. The CFSR and TRMM rain rates are analyzed for 12 winters from 1998 to 2010, and EC–YOTC is examined for two winters from 2008 to 2010. Since the MJO circulation is dominated by the zonal wind, our primary focus in this study is confined to the role of CMT by various spatial–temporal scales on the zonal momentum budget of the MJO.

b. Methods

The tendency equation for the zonal wind on a model grid in pressure coordinates can be written as follows:

$$\frac{\partial u}{\partial t} = -u\frac{\partial u}{\partial x} - v\frac{\partial u}{\partial y} - \omega\frac{\partial u}{\partial p} + f(y)v - \frac{\partial \varphi}{\partial x} + X, \quad (1)$$

where u and v are the zonal and meridional components of wind, respectively; ω is the vertical pressure velocity; f is the Coriolis parameter; and φ is geopotential height. The time rate of change of the zonal wind (acceleration or deceleration) because of unresolved physical subgrid-scale processes, including the CMT, vertical diffusion, and gravity wave drag, as well as a nonphysical increment term induced at each reanalysis cycle is given by X. By employing a residual momentum budget analysis approach, previous studies suggested that CMT could be the most dominant subgrid-scale process in the free troposphere over the tropical oceans (Carr and Bretherton 2001; Tung and Yanai 2002a; Lin et al. 2005). However, accurate estimates of the subgrid-scale CMT term by using the residual budget analysis greatly suffer from large uncertainties in several reanalysis fields, including vertical velocity and geopotential height, which do not have direct observational constraints, as well as the reanalysis incremental term, which often can be comparable to physical terms in amplitude (e.g., Kiranmayi and Maloney 2011; Mapes and Bacmeister 2012). Hence, in this study, instead of using a residual budget analysis for the momentum, we take advantage of the parameterized CMT fields archived from both CFSR and EC–YOTC to represent the subgrid-scale CMT.

In general, the subgrid-scale cumulus effect on environmental momentum can be represented as below, following Shapiro and Stevens (1980):

$$\frac{\partial \mathbf{V}}{\partial t} = -M_c\frac{\partial \mathbf{V}}{\partial p} + \delta(\mathbf{V}_c - \mathbf{V}) + \sigma\left(\frac{1}{\rho}\nabla p^*\right), \quad (2)$$

where $\mathbf{V}$ represents the environmental (grid scale) wind, $\mathbf{V}_c$ is the wind in the cloud, M_c is the cloud mass flux, δ is the mass detrainment at the cloud boundaries, ρ is density, p^* is the convection-induced pressure perturbation, and σ is the fractional area covered by cumulus clouds. The first term on the right-hand side represents the environmental momentum field through the part of

environmental vertical motion compensating convective mass flux, which depends on the environmental wind shear and magnitude of the convective mass flux. The second term stands for the detrainment of excess momentum from clouds, and the third term stands for the convection-induced pressure gradient force. All three of these CMT effects were considered in the version of the GFS model used for the CFSR, with the third effect being taken into account by empirically increasing the entrainment for momentum in the updraft (Moorthi et al. 2001). A similar treatment of subgrid-scale CMT was also adopted in the Cy31r1 version of the ECMWF model that was used for the EC–YOTC analysis.[1]

To quantify the significance of the subgrid-scale CMT associated with the MJO with respect to the momentum transport at model grid scales, we examine the advection terms on the right-hand side of Eq. (1). Additionally, the contribution by mesoscale systems to the total grid-scale CMT is also assessed following an approach by Miyakawa et al. (2012). For this purpose, the total variable u is assumed to be decomposed into large-scale $\overline{u}$ and mesoscale u' components (e. g. , $u = \overline{u} + u'$). The large-scale circulation component is derived by the horizontal averaged value within a 5° radius of circular area, while the mesoscale circulation at each grid point is obtained by the deviation from the circular mean. Following Miyakawa et al. (2012), a radius of 5° of circular area was chosen so that it is large enough and that the stratiform along with convective regions accompanied by MCSs can be captured as the vertical redistribution of momentum by an MCS that is closely related to the stratiform region (Yang and Houze 1996; Houze 2004). Sensitivity tests were conducted by slightly changing the radius from 3° to 7° for the scale separation, but results did not change significantly.

The total grid-scale advection terms on the rhs of Eq. (1), which consist of zonal, meridional, and vertical components, can be further partitioned into[2]

$$-\frac{\partial uu}{\partial x} \approx -\frac{\partial \overline{u}\,\overline{u}}{\partial x} - \frac{\partial u'u'}{\partial x}, \tag{3}$$

$$-\frac{\partial uv}{\partial y} \approx -\frac{\partial \overline{u}\,\overline{v}}{\partial y} - \frac{\partial u'v'}{\partial y}, \quad \text{and} \tag{4}$$

$$-\frac{\partial u\omega}{\partial p} \approx -\frac{\partial \overline{u}\,\overline{\omega}}{\partial p} - \frac{\partial u'\omega'}{\partial p}. \tag{5}$$

The first terms on the right-hand side are the large-scale momentum tendency, and the second terms are mesoscale momentum tendency. Several previous studies have suggested that eddy horizontal momentum transport terms are much smaller than the eddy vertical transport (Carr and Bretherton 2001; Tung and Yanai 2002a,b; Lin et al. 2008), which is also to be shown in the following for the mesoscale momentum tendency.

The real-time multivariate MJO (RMM) index by Wheeler and Hendon (2004) (data downloaded from http://cawcr.gov.au/staff/mwheeler/maproom/RMM/, accessed July 2013) is adopted for the MJO-cycle composite analysis. The RMM index is derived by the empirical orthogonal function (EOF) analysis of combined fields of equatorially averaged 850- and 200-hPa zonal winds and outgoing longwave radiation (OLR). The pair of two leading principal component time series (i.e., RMM1 and RMM2) defines a two-dimensional phase space of the MJO, and each phase approximately indicates the location of the MJO convection within its life cycle. MJO life cycle composites can then be obtained by averaging a given variable over each of eight MJO phases in which the amplitude of the MJO (defined as $\sqrt{\mathrm{RMM}_1^2 + \mathrm{RMM}_2^2}$) is greater than unity.

3. Results

a. *Vertical subgrid-scale CMT structure associated with the MJO*

Before examining the detailed CMT structure associated with the MJO, the fidelity of the CFSR in representing the MJO is first illustrated by comparing the MJO life cycle composite of precipitation based on the CFSR against that by the TRMM observations (Fig. 1). Prior to compositing, daily rainfall fields are first derived based on the 6-hourly CFSR and the 3-hourly TRMM datasets, and are then subjected to bandpass filtering to retain periods of 20–90 days after removal of the climatological annual cycle. For the MJO life cycle composite based on 12 winters from 1998 to 2010, there are about 172 strong MJO days on average for each MJO phase. The composite evolution patterns of anomalous rainfall during the eight MJO phases based on TRMM (Fig. 1a) clearly illustrate the origin of the MJO convection over the western IO and its eastward propagation. Although slightly weaker amplitudes in rainfall anomalies are noted in the CFSR composite (Fig. 1b), the eastward propagation as well as the observed phase speed of the MJO is well represented in the CFSR rainfall field, which suggests that the CFSR captures convection signals associated with the MJO quite well. Since CFSR rainfall is consistent with many other variables generated from the reanalysis model, particularly the CMT fields as the focus of this study, in the following, we will mainly use CFSR

[1] See http://old.ecmwf.int/research/ifsdocs/CY31r1/index.html.

[2] On the spatial–temporal scale of the MJO, correlations between a large- and mesoscale quantity are small in general.

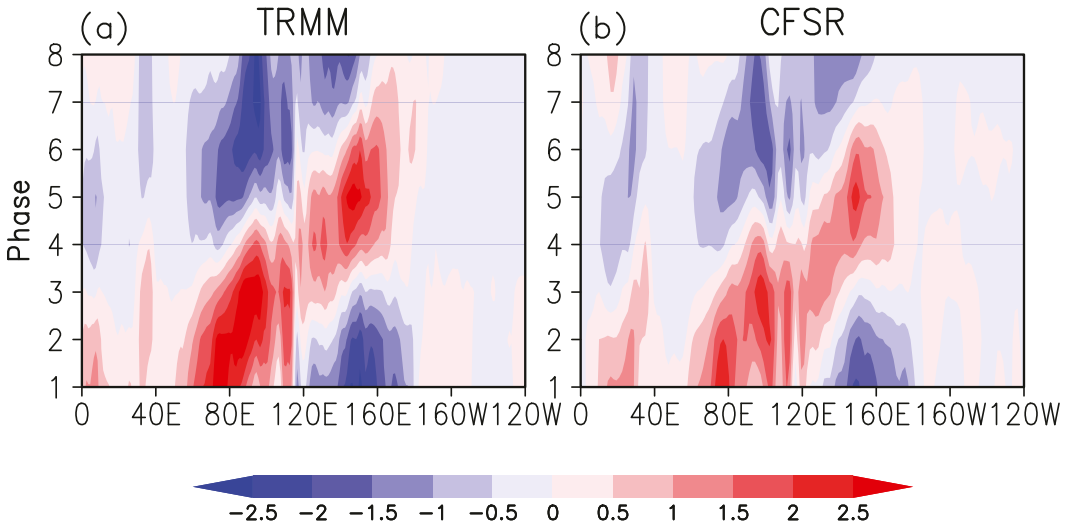

FIG. 1. MJO phase–lon diagrams of composite precipitation anomalies (mm day^{-1}) based on (a) TRMM and (b) CFSR. MJO phases are derived from the MJO life cycle composite based on the RMM index and rainfall anomalies are averaged between 5°S and 5°N.

rainfall data to derive an MJO index to characterize the vertical CMT structure associated with the MJO.

A linear regression approach is used to derive vertical profiles of various fields related to the MJO. Similar results can be obtained if a composite analysis is applied to these fields based on selected strong MJO events. For regression calculations, MJO indices over the IO and WP are defined by domain-averaged 20–90-day bandpass–filtered rainfall anomalies over the IO (5°S–5°N, 75°–85°E) and WP (5°S–5°N, 150°–160°E) and normalized by their corresponding standard deviations, respectively. Then, the three-dimensional structures associated with the MJO over the IO and WP are derived based on linear regressions between the time series of different 3D variables (predictand) and the corresponding MJO indices (predictor).

Figure 2 depicts daily averaged subgrid-scale CMT (shaded), along with 20–90-day bandpass–filtered wind (vectors with components u and $-\omega$) and rainfall anomalies (green line and right y axis) based on the CFSR, by regressing against the IO (Fig. 2a) and WP (Fig. 2b) MJO indices. A baroclinic structure in anomalous wind fields associated with the MJO is clearly evident over both the IO and WP, with westerly (easterly) wind anomalies to the west (east) of the convective center in the lower troposphere and a reversed circulation at the upper level. In the CMT fields associated with the MJO over the IO, a three-layer structure in subgrid-scale momentum tendency (shaded; Fig. 2a), with a positive sign in the upper troposphere (300–100 hPa), a negative center in the midtroposphere (700–300 hPa), and another positive center below 700 hPa, although rather weak, is evident under and west of the MJO convection center (west of 100°E). A three-layer structure in momentum tendency, but with an opposite sign, is also noted to the east of 100°E in Fig. 2a. Similar vertical profiles in subgrid-scale momentum tendency corresponding to enhanced MJO convection can also be discerned over the WP (Fig. 2b), although the amplitude in momentum tendency to the east of the convection is rather weak compared to its IO counterpart.

Figure 3 further illustrates horizontal distributions of the regressed subgrid-scale anomalous momentum tendency patterns onto the IO (Figs. 3a–c) and WP (Figs. 3d–f) MJO indices at 200, 500, and 900 hPa, respectively. Also superimposed on these plots are the corresponding regressed rainfall anomalies by green contours. A three-layer structure in subgrid-scale momentum tendency is again readily seen in regression patterns based on both the IO and WP rainfall indices. When the enhanced MJO is located over the IO, positive momentum tendency anomalies over 200 hPa are slightly shifted to the west side of the enhanced MJO envelope, while a negative momentum tendency prevails over a large area to the east and on both sides of enhanced MJO away from the equator (Fig. 3a).

On the first-order approximation, the u-momentum tendency induced by subgrid-scale CMT as illustrated in Fig. 2 will damp the MJO circulation in the free atmosphere above 700 hPa, since the low- to midlevel negative (positive) momentum tendency to the west (east) of the MJO convection center will reduce the westerly (easterly) anomalous wind associated with the MJO; similarly, in the upper troposphere, the positive (negative) momentum tendency to the west (east) side of the MJO

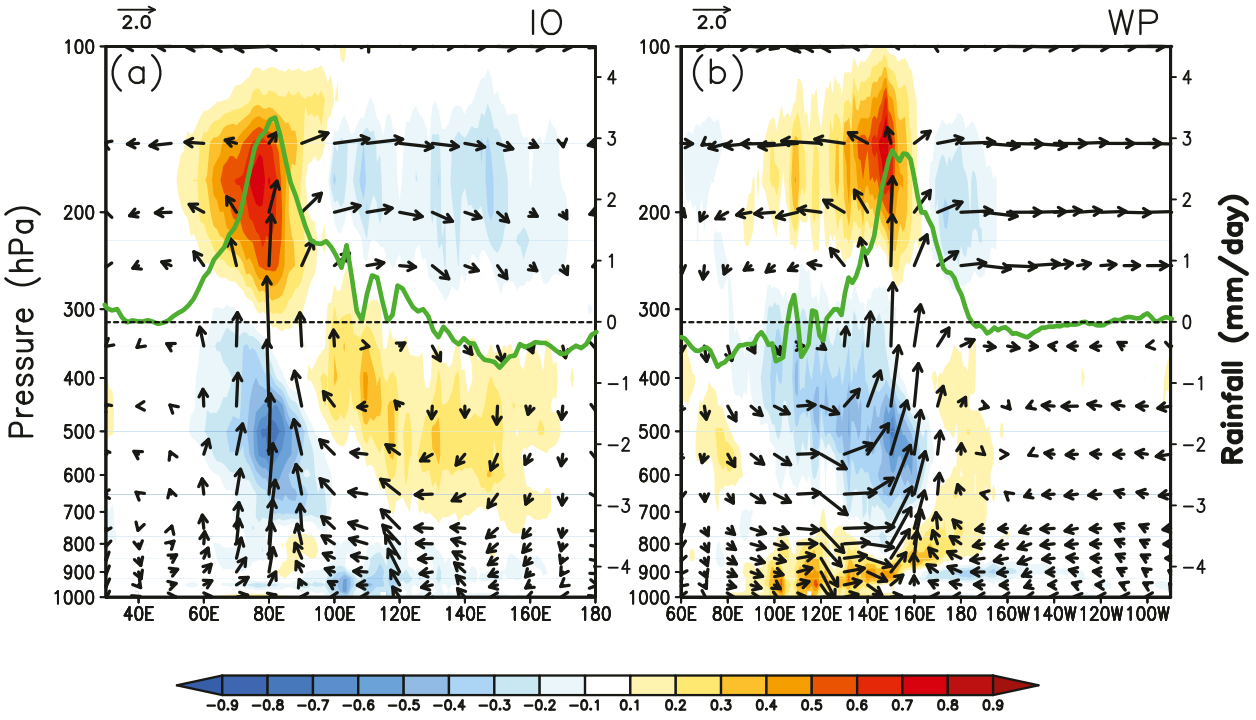

FIG. 2. Lon–height cross section of subgrid-scale momentum tendency regressed onto the (a) IO and (b) WP MJO indices. Shading shows the regressed subgrid-scale momentum tendency (m s^{-1} day^{-1}), and green lines depict the 20–90-day bandpass–filtered precipitation (mm day^{-1}; right y axes). Vectors denote the 20–90-day bandpass–filtered wind vectors for which the horizontal component is the zonal wind (m s^{-1}), and the vertical component is the pressure velocity (Pa s^{-1} multiplied by a factor of −100). All values are averaged between 5°S and 5°N.

center is also against the MJO circulation. However, the lowest branch of the three-layer momentum tendency structure between the surface and 700 hPa—namely, positive (negative) momentum tendencies to the west (east)—enhance the MJO circulation, particularly, over the WP (Fig. 2b). Since the sustenance of tropical deep convection largely relies on moisture convergence in the planetary boundary layer (PBL) and lower troposphere (Sherwood 1999), the momentum tendency structure attributable to the subgrid-scale cumulus effect, as suggested in Fig. 2, could exert important influences on the MJO by affecting the coupling between circulation and convection [e.g., the gross moist stability (Neelin and Held 1987; Raymond et al. 2009)].

On the other hand, as illustrated by Figs. 2 and 3, the strongest anomalous CMT signals in both the mid- (~500 hPa; negative sign) and upper (~200 hPa; positive sign) troposphere are largely collocated with the MJO convection center. This u-momentum tendency will induce an east–west asymmetric divergence tendency relative to the MJO convection center. A similar regression pattern against the IO MJO rainfall index as in Fig. 2a, but for the longitude–height cross section of zonal convergence of the subgrid-scale momentum tendency, is displayed in Fig. 4a. Additionally, the horizontal divergence patterns of the subgrid-scale u-momentum tendency at different vertical levels are displayed in Figs. 4b–d. It is clearly shown that a maximum divergence (convergence) tendency is located about 10° east (west) of the convection center in the lower to midtroposphere, with an opposite sign in the upper levels, suggesting a tendency in generating a secondary circulation in the free troposphere with downward (upward) motion to the east (west) of the MJO center. This tendency in divergence and associated secondary circulation by the subgrid-scale momentum tendency near the MJO center could act as a drag on the eastward propagation of the MJO, which is in accord with previous GCM studies that inclusion of CMT effects in a GCM will reduce the eastward phase speed of the MJO in the model (e.g., Deng and Wu 2010). On the other hand, the divergence tendency in the PBL due to subgrid-scale processes shows a convergence (divergence) tendency to the east (west) of the MJO center (Fig. 4d). As a result, this tendency in generating upward (downward) motion to the east (west) of the MJO could enhance the eastward propagation of the MJO in the PBL, therefore possibly contributing to the vertical tilt structure of the MJO to some degree, although the observed vertical tilting structure of the MJO might be ascribed to multicloud development during MJO evolution (e.g., Majda and

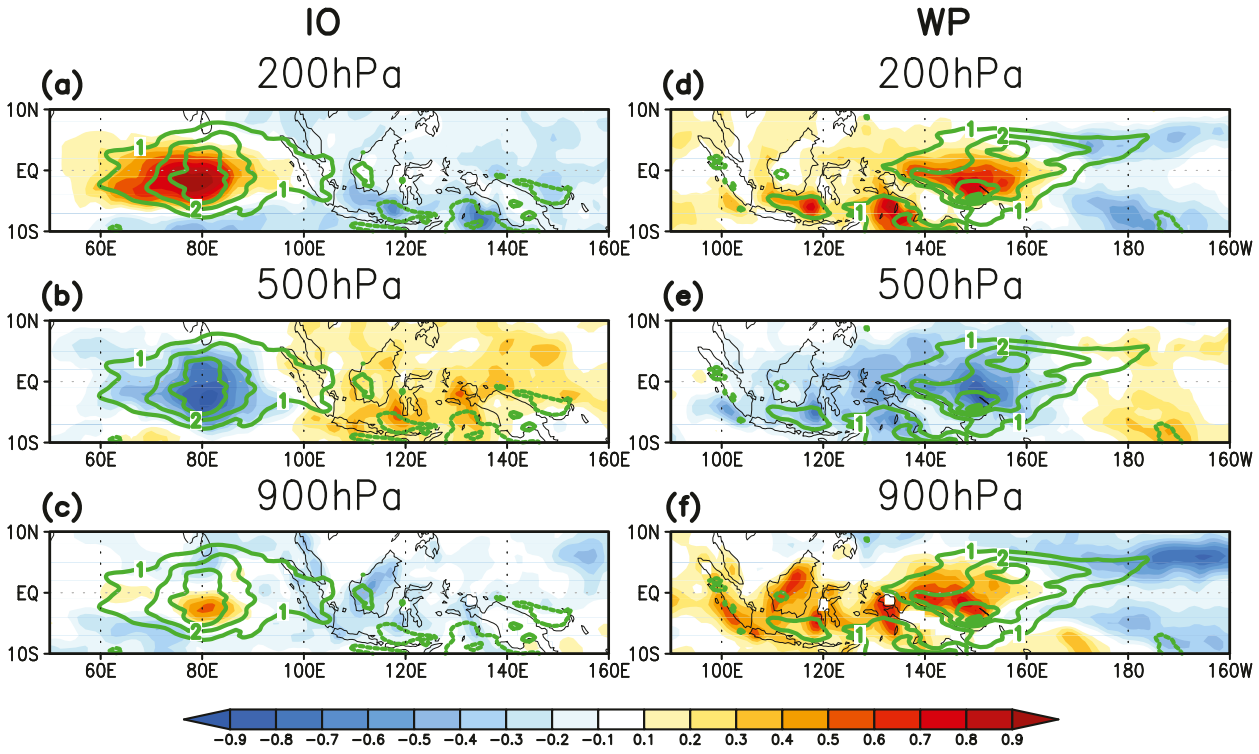

FIG. 3. Spatial patterns of regressed subgrid-scale momentum tendency (m s^{-1} day^{-1}; shading) at (a),(d) 200; (b),(e) 500; and (c),(f) 900 hPa, and 20–90-day bandpass–filtered precipitation anomalies (mm day^{-1}; green contour) onto the (left) IO and (right) WP MJO indices.

Biello 2004; Mapes et al. 2006). It is of particular interest to note that this three-layer structure in the subgrid-scale momentum tendencies corresponding to MJO convection over both IO and WP in Fig. 2 closely resembles the composite mesoscale momentum tendency profiles based on CRM simulations in Miyakawa et al. (2012). Since composite analysis was conducted relative to MJO convection over the WP in Miyakawa et al. (2012), the CMT effects were mainly found to the west of the convection center, which is also the case in our regressed CMT pattern over the WP (Fig. 2b). The amplitude of the subgrid-scale momentum tendencies associated with the MJO is also comparable to that of mesoscale tendencies based on CRM simulations. Similar effects by the mesoscale CMT, as mentioned above, were also discussed in Miyakawa et al. (2012).

b. *Grid-scale momentum transport associated with the MJO*

In this subsection, momentum transport associated with the MJO as a result of grid-scale circulation based on the CFSR is examined. One particular question we address is the effect of synoptic-scale waves on the MJO momentum budget compared to that of the subgrid-scale processes examined in the previous section. While we are well aware that organized mesoscale circulations with a scale of hundreds of kilometers (e.g., Houze 2004) are only marginally resolved (permitted) by the 50-km CFSR data, vertical CMT profiles of u momentum due to mesoscale systems are explored following the spatial filtering approach utilized by Miyakawa et al. (2012), as previously described. Total u-momentum tendencies associated with the MJO because of grid-scale advection terms in Eq. (1) can then be separated into mesoscale and the remaining large-scale components, as in Eqs. (3)–(5).

To demonstrate how the mesoscale spatial filtering approach works, Fig. 5 illustrates a map of the standard deviations of the mesoscale rainfall. Because of the 50-km resolution of CFSR data, the mesoscale rain subject to the spatial filtering will largely represent very large-scale MCSs, as well as some small synoptic systems. It should also be mentioned that the scale separation based on the 5°-radius circular average, while useful, is somewhat arbitrary, because the MCSs have no natural cutoff size (Yuan and Houze 2010). Nevertheless, the spatial distribution of the mesoscale rain variability shown in Fig. 5 largely captures major MCS activity centers, as revealed by remote sensing observations (e.g., Schumacher and Houze 2003; Yuan and Houze 2010). For example, the largest standard deviations of mesoscale rainfall over the Maritime Continent and adjacent oceans are likely

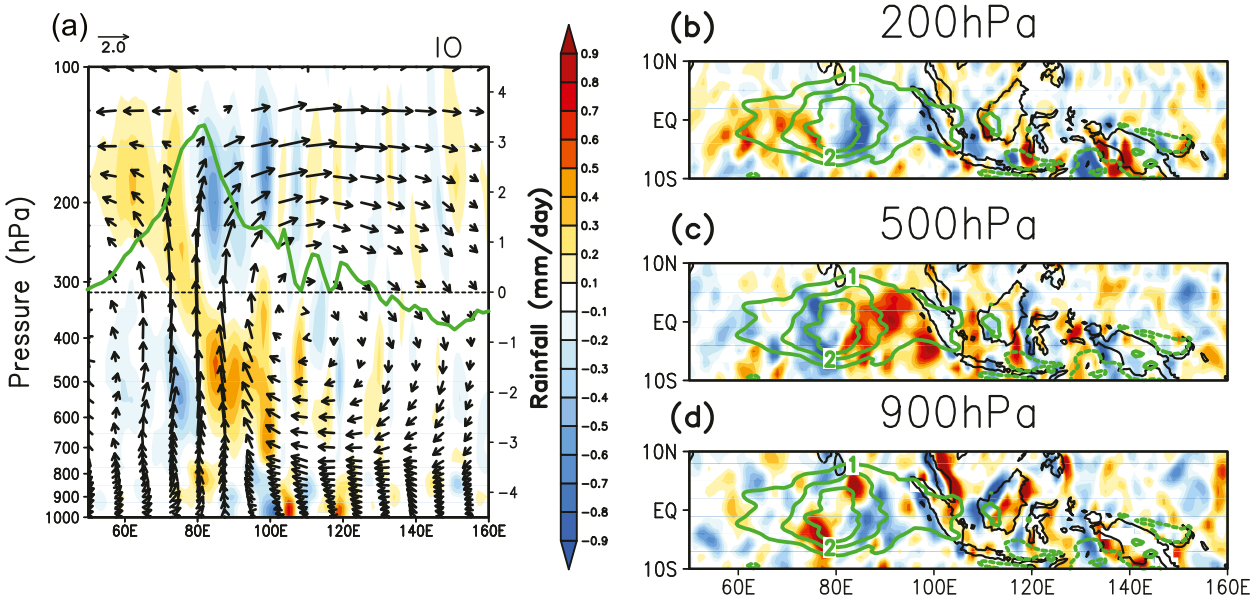

FIG. 4. (a). As in Fig. 2a, but for zonal divergence of subgrid-scale momentum tendency (10^{-6} s^{-1} day^{-1}; shading). (b)–(d) As in Figs. 3a–c, but for zonal divergence of subgrid-scale CMT (10^{-6} s^{-1} day^{-1}; shading).

associated with a vigorous diurnal cycle of convection and associated propagating gravity waves (Yang and Slingo 2001; Rauniyar and Walsh 2011). Meanwhile, strong MCS activity occurs over the WP along the intertropical convergence zone (ITCZ) and South Pacific convergence zone (SPCZ), consistent with MCSs identified by Yuan and Houze (2010) based on satellite estimates. Therefore, it is reasonable to apply the spatial filtering to isolate MCSs from the large-scale environment. A similar spatial separation approach is then applied to horizontal wind and vertical velocity fields. Vertical profiles of momentum transport associated with the MJO because of MCSs, as well as the remaining large-scale circulation, are calculated based on Eqs. (3)–(5).

Figure 6 displays longitude–height plots of vertical u-momentum transport by total grid-scale circulation (Figs. 6a,d), and its separation into mesoscale (Figs. 6b,e) and remaining large-scale (Figs. 6c,f) components corresponding to Eq. (5). Note that these vertical profiles are also derived by regression against the IO (Figs. 6a–c) and WP (Figs. 6d–f) MJO indices. In the total vertical grid-scale u-momentum transport fields, the three-layer vertical structure, as previously noted in the subgrid-scale momentum tendency, is again clearly evident in both regressed patterns over the IO (Fig. 6a) and WP (Fig. 6d), but with an opposite sign. To the west (east) of the MJO center, negative (positive) momentum tendency anomalies are present in the upper level, positive (negative) anomalies are present at the midlevel, and negative (positive) anomalies are present again in the lower troposphere, with a comparable magnitude to that of the subgrid-scale tendency. Additionally, very similar to

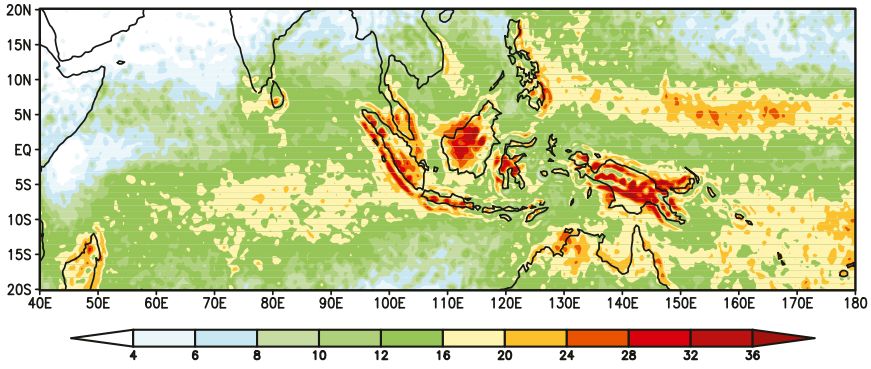

FIG. 5. Std dev of the mesoscale rain derived by the spatial scale separation (mm day^{-1}) based on the CFSR for 12 winters (NDJFMA).

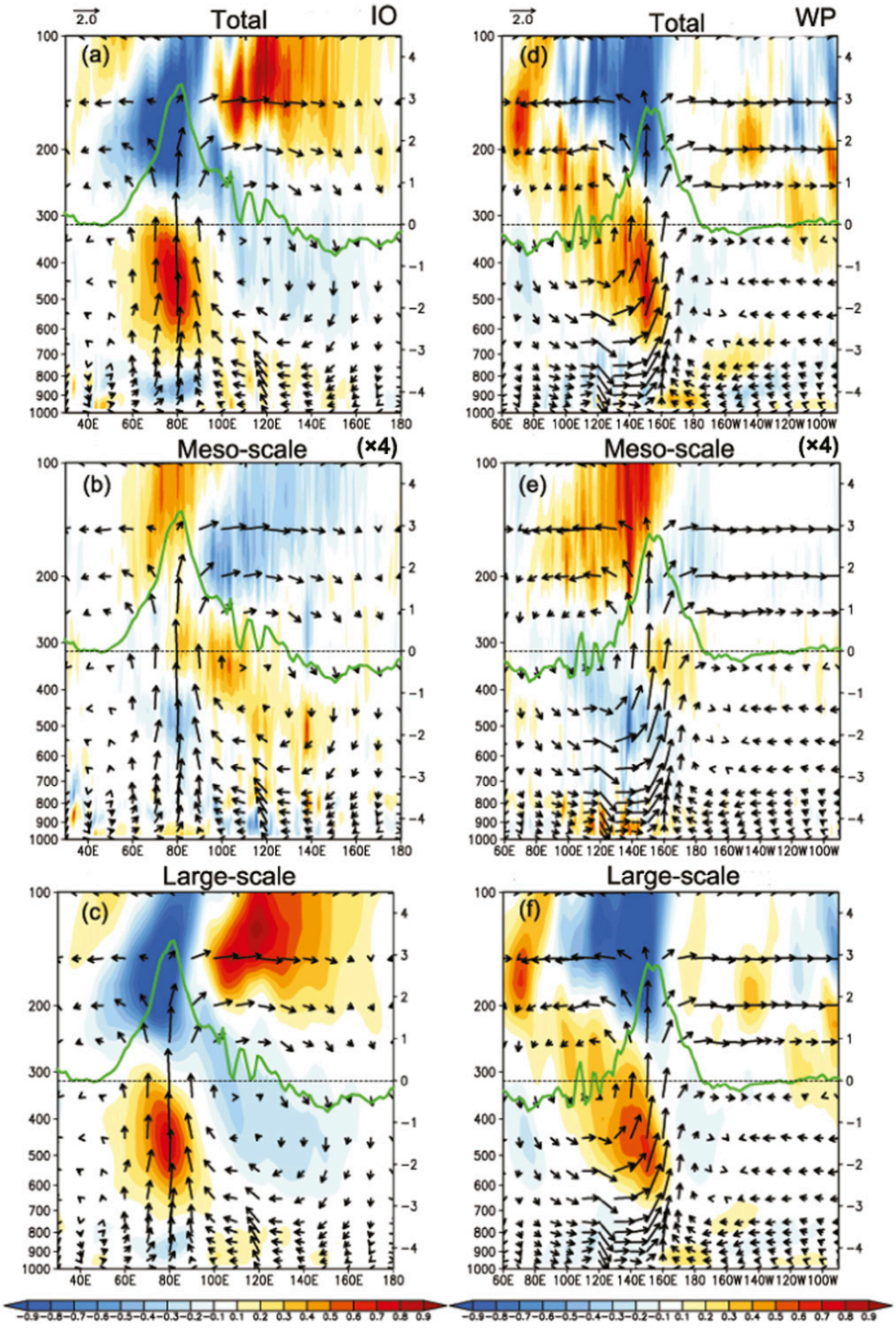

FIG. 6. Lon–height plots of 5°S–5°N averaged grid-scale u-momentum tendency (m s^{-1} day^{-1}) by (a),(d) total grid-scale vertical momentum transport $-\partial(u\omega)/\partial p$; (b),(e) mesoscale CMT $-\partial(u'\omega')/\partial p$; and (c),(f) large-scale momentum transport $-\partial(\overline{u}\,\overline{\omega})/\partial p$ regressed onto the (left) IO and (right) WP MJO indices. For the sake of comparison, $-\partial(u'\omega')/\partial p$ is multiplied by a factor of 4. The green lines and vectors are as in Fig. 2, denoting corresponding regressed rainfall anomalies (mm day^{-1}) and circulations.

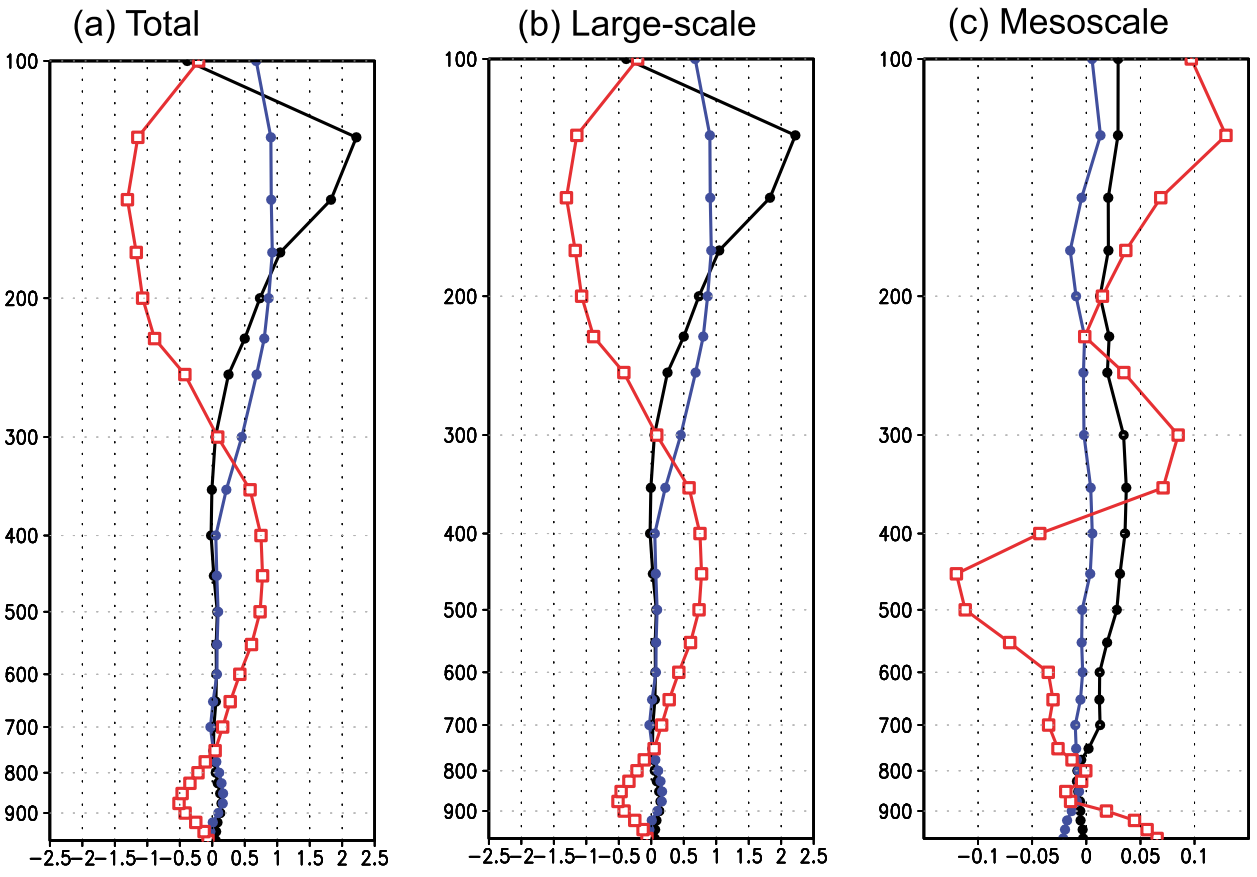

FIG. 7. Vertical profiles of u-momentum tendencies (m s^{-1} day^{-1}) by zonal (black), meridional (blue), and vertical (red) transports by (a) total grid-scale, (b) large-scale, and (c) mesoscale circulations, based on the regression onto the IO MJO index. Note the different scale on the x axis of (c). All variables are averaged over 5°S–5°N, 75°–85°E.

that in the subgrid-scale momentum tendency profile (Fig. 2b), the total grid-scale tendency pattern over the WP exhibits a strong amplitude to the west of the MJO center, in contrast to the rather-weak amplitude on the east side (Fig. 6d). The decomposition of the total grid-scale vertical u-momentum transport suggests that the amplitude of the mesoscale vertical CMT transport is comparatively very weak (note the different coloring scales for Figs. 6b,e); namely, the total grid-scale vertical u-momentum transport is dominated by the large-scale transport. The rather-weak mesoscale momentum tendency compared to the total grid-scale tendency is not unexpected because of the relatively coarse spatial (50 km) and temporal (6 hourly) resolutions of the CFSR that cannot adequately resolve mesoscale systems. Regardless of its weak amplitude, however, a similar three-layer vertical pattern is also evident in the mesoscale momentum tendency profiles (Figs. 6b,e), resembling the subgrid-scale CMT structure shown in Fig. 2, and also in agreement with the mesoscale momentum tendency profiles based on CRM simulations in Miyakawa et al. (2012).

A comparison of vertical profiles in u-momentum transport by total, large-scale, and mesoscale circulations over the IO is further provided in Fig. 7. In addition to the vertical u-momentum transport associated with the MJO (red curves), vertical profiles of zonal (black) and meridional (blue) transport of u momentum [refer to Eqs. (3)–(5)] are also shown in Fig. 7. Again, compared to the large-scale vertical u-momentum transport, the amplitude of the mesoscale momentum tendency is rather weak; the total grid-scale tendency is mainly contributed by the large-scale transport for both horizontal and vertical transport. Further shown in Fig. 7c is that zonal and meridional components of mesoscale u-momentum transport are weak compared to the vertical mesoscale CMT component. This is consistent with the result of Miyakawa et al. (2012), as well as previous subgrid-scale CMT estimates based on reanalysis datasets (e.g., Carr and Bretherton 2001; Tung and Yanai 2002a,b). In contrast, for the large-scale u-momentum transport (Fig. 7b), both zonal (black) and meridional (blue) transports exhibit comparable amplitude to the vertical

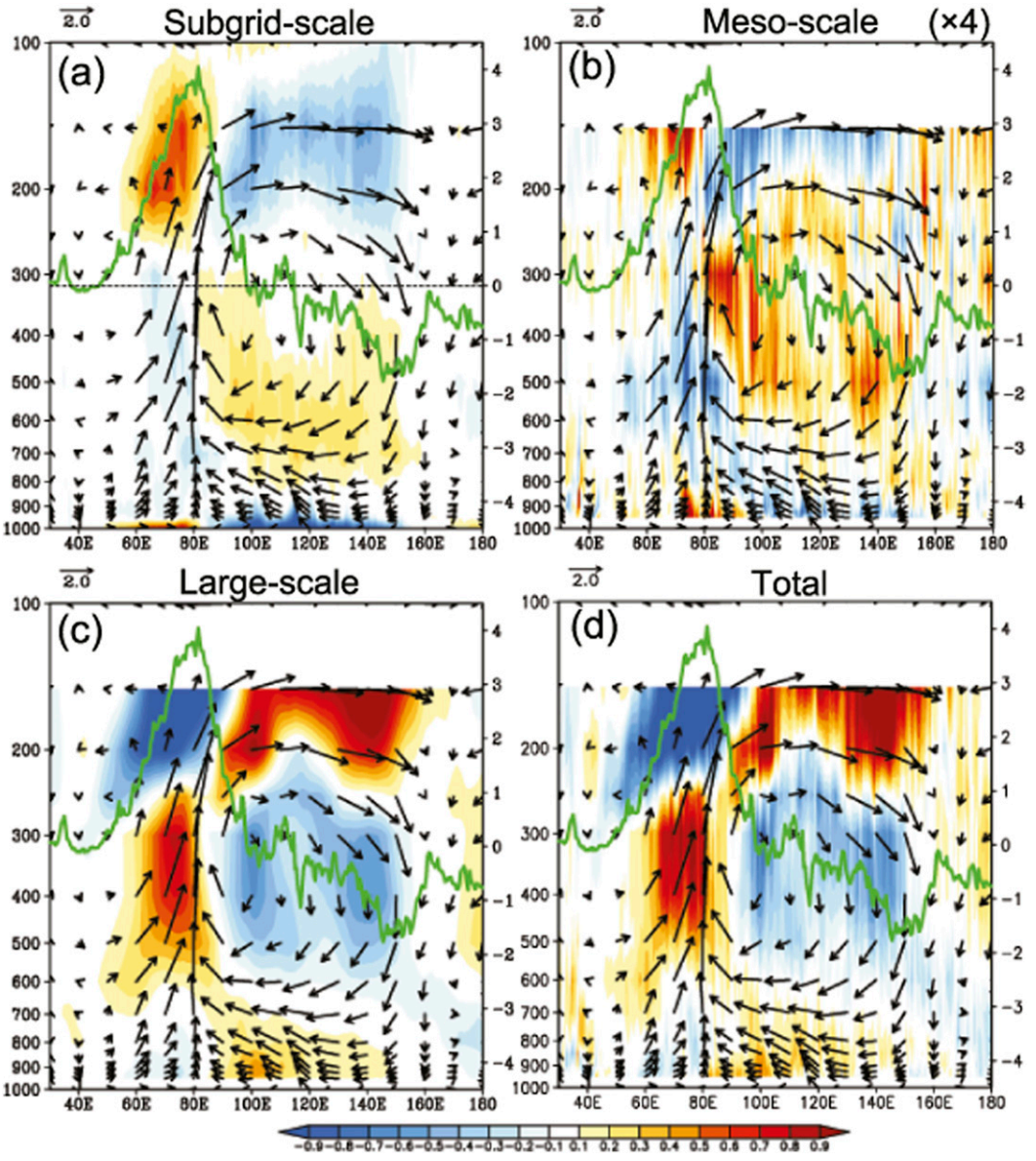

FIG. 8. Lon–height plots of momentum tendency based on the EC–YOTC reanalysis (m s^{-1} day^{-1}; shading) by (a) subgrid-scale, (b) mesoscale, (c) large-scale, and (d) total grid-scale vertical transports derived by regressions onto the IO MJO index. The mesoscale momentum tendency in (b) is multiplied by a factor of 4. The green lines and vectors are as in Fig. 2, but are based on the EC–YOTC analysis. All values are averaged between 5°S and 5°N.

component, particularly in the upper troposphere between 300 and 100 hPa. Both large-scale horizontal transport components tend to counteract the vertical transport. This is also largely consistent with CRM results in Miyakawa et al. (2012, their Fig. 13). Similar results are found in regressed *u*-momentum transport profiles over the WP (not shown).

To further substantiate the results based on the CFSR, we analyzed the EC–YOTC reanalysis following the same approach applied to the CFSR. Figure 8 displays longitude–pressure cross-sectional profiles of momentum tendency by subgrid-scale (Fig. 8a), mesoscale (Fig. 8b), large-scale (Fig. 8c), and total grid-scale vertical transports (Fig. 8d), based on the EC–YOTC data. Although differences are discernible between these two datasets, particularly in the subgrid-scale CMT profiles, which are possibly because of relatively short sampling of the EC–YOTC data, as well as differences in deriving the cloud mass fluxes in these two reanalysis models, the vertical CMT structure corresponding to each component derived by EC–YOTC exhibits great similarity to the CFSR results, including the three-layer vertical structure of the

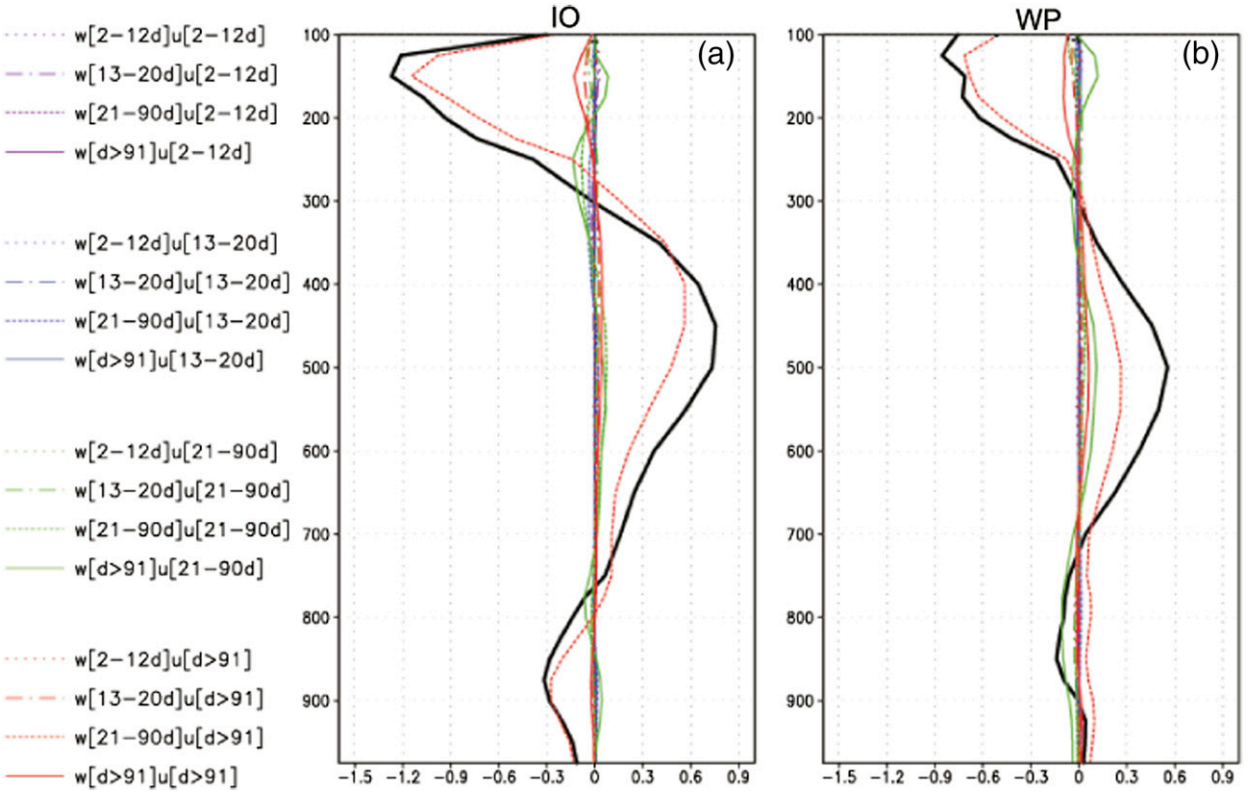

FIG. 9. Vertical profiles of large-scale u-momentum tendency (m s^{-1} day^{-1}) as a result of vertical transport by circulations on various time scales based on regressions against the (a) IO and (b) WP MJO indices. Values are averaged over 5°S–5°N, 75°–85°E in (a) and 5°S–5°N, 150°–160°E in (b). The black solid lines represent total large-scale vertical transports.

momentum tendencies, the opposite sign of the subgrid- and grid-scale tendencies, and the dominance of the large-scale contribution to the total grid-scale tendency. This remarkable similarity lends further confidence to the CMT patterns associated with MJO derived from the CFSR.

c. *Role of different time scales on the total large-scale momentum transport*

Roles of different temporal scales on the total large-scale vertical u-momentum transport profiles of the MJO are further analyzed based on the CFSR in this subsection. We decompose the remaining large-scale $[\overline{u}]$ and $[\overline{\omega}]$ fields, subsequent to the removal of mesoscale circulations from the total grid-scale fields, into four different time scales: namely, 2–12 (synoptic band), 13–20 (high-frequency intraseasonal band), 21–90 (intraseasonal band), and beyond 91 days (winter mean state) by applying a Lanczos bandpass filter (Duchon 1979). The vertical profiles of the resultant 16 terms of large-scale vertical u-momentum transport $-\partial[\overline{u}][\overline{\omega}]/\partial p$, through different combinations of time-filtered $[\overline{u}]$ and $[\overline{\omega}]$, are shown in Figs. 9a and 9b for the IO and WP. The cutoff frequencies for each variable are denoted in the legend of Fig. 9. It is noteworthy that these different time-scale bands as isolated by the bandpass filtering could not be completely exclusive from each other because of slight overlap in the tails between neighboring bands. Sensitivity tests suggest that results will not be significantly changed by using a different bandpass filtering method or by adopting slightly different cutoff frequencies. Among these 16 terms, the contribution of $-\partial[\overline{u}]_{>91\mathrm{d}}[\overline{\omega}]_{21-90\mathrm{d}}/\partial p$, the vertical transport of u with a period longer than 91 days by the MJO-scale vertical motion (red-dashed line in Fig. 9), accounts for the dominant role for the total large-scale vertical u-momentum transport (black thick line) over both the IO and WP, although a relatively smaller contribution (about 50%) to the total large-scale momentum tendency is noted over the WP, particularly in the low to midlevels between 700 and 300 hPa (Fig. 9b). Vertical u-momentum transport by synoptic time-scale waves, which has been proposed to play a critical role for the MJO in recent idealized model studies, however, does not significantly contribute to the total grid-scale momentum, as suggested by the CFSR.

Since the $-\partial[\overline{u}]_{>91\mathrm{d}}[\overline{\omega}]_{21-90\mathrm{d}}/\partial p$ term plays such a critical role in the total large-scale momentum tendency over

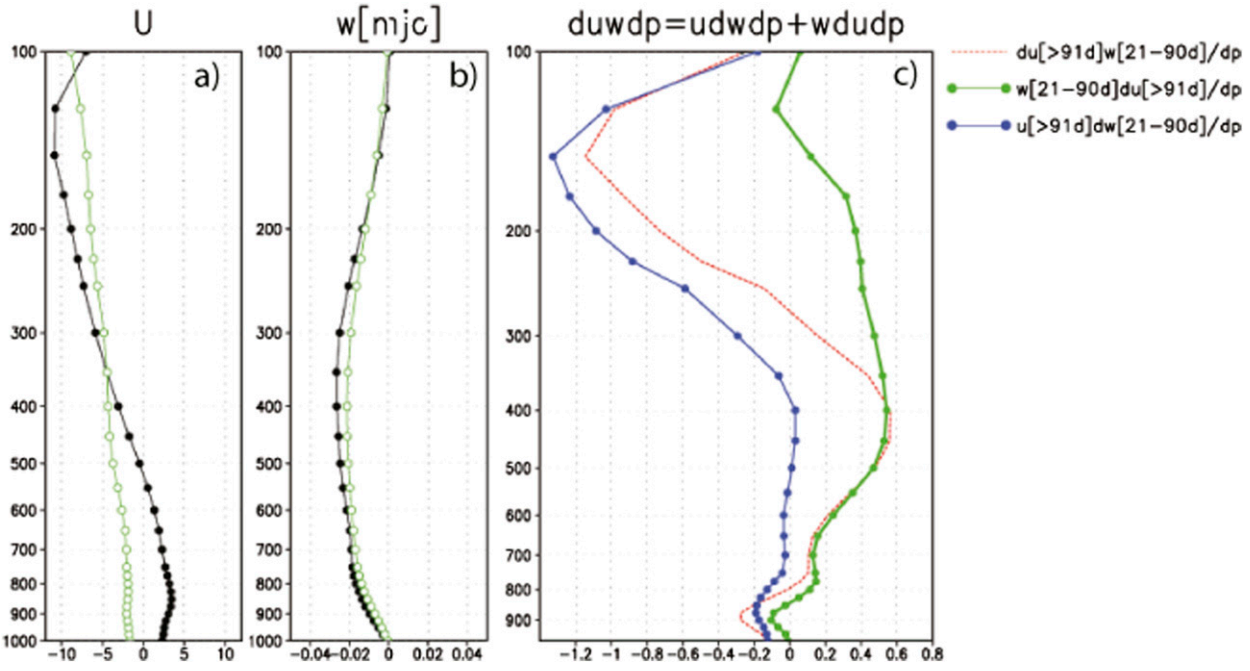

FIG. 10. Vertical profiles of (a) winter mean u ($\mathrm{m\,s^{-1}}$) and (b) 21–90-day bandpass–filtered vertical pressure velocity ($\mathrm{Pa\,s^{-1}}$) regressed against the IO (5°S–5°N, 75°–85°E; black) and the WP (5°S–5°N, 150°–160°E; green) MJO indices. (c) The $-\partial\{[\overline{u}]_{>91\mathrm{d}}[\overline{\omega}]_{21-90\mathrm{d}}\}/\partial p$ term over the IO ($\mathrm{m\,s^{-1}\,day^{-1}}$; red-dashed line; duplicated from Fig. 9a), and its decomposition into $-[\overline{\omega}]_{21-90\mathrm{d}}\partial[\overline{u}]_{>91\mathrm{d}}/\partial p$ (green) and $-[\overline{u}]_{>91\mathrm{d}}\partial[\overline{\omega}]_{21-90\mathrm{d}}/\partial p$ (blue).

both the IO and WP, Fig. 10 further displays vertical profiles of the winter mean zonal wind component $[\overline{u}]_{>91\mathrm{d}}$ (Fig. 10a), and the vertical pressure velocity associated with the MJO $[\overline{\omega}]_{21-90\mathrm{d}}$ (Fig. 10b), over the IO (black) and WP (green), respectively. The winter mean zonal winds over both the IO and WP are characterized by easterly vertical shear (although a much weaker shear over the WP) with maximum easterlies and westerlies near 150 and 850 hPa, respectively. Meanwhile, the vertical velocity associated with the MJO over both regions is characterized by anomalous upward motion with a maximum near 350 hPa, in agreement with the enhanced MJO convection.

To further understand the three-layer profiles in large-scale CMT, the term $-\partial\{[\overline{u}]_{>91\mathrm{d}}[\overline{\omega}]_{21-90\mathrm{d}}\}/\partial p$ is further decomposed into two terms and shown in Fig. 10c: $-[\overline{\omega}]_{21-90\mathrm{d}}\partial[\overline{u}]_{>91\mathrm{d}}/\partial p$ (green) and $-[\overline{u}]_{>91\mathrm{d}}\partial[\overline{\omega}]_{21-90\mathrm{d}}/\partial p$ (blue). Our results suggest that both of these terms contribute to the three-layer vertical structure in $-\partial\{[\overline{u}]_{>91\mathrm{d}}[\overline{\omega}]_{21-90\mathrm{d}}\}/\partial p$ (red-dashed line, as duplicated from Fig. 9a); while the $-[\overline{u}]_{>91\mathrm{d}}\partial[\overline{\omega}]_{21-90\mathrm{d}}/\partial p$ term (blue) is mainly responsible for the negative grid-scale momentum tendency in the upper troposphere, the term $-[\overline{\omega}]_{21-90\mathrm{d}}\partial[\overline{u}]_{>91\mathrm{d}}/\partial p$ (green) is important for the positive anomalies in the low to midlevels. Both of these terms contribute to relatively weak negative momentum tendency anomalies near the surface. Moreover, the weaker mean easterly vertical wind shear over the WP compared to that over the IO, as shown in Fig. 10a, and thus a weaker amplitude in $-[\overline{\omega}]_{21-90\mathrm{d}}\partial[\overline{u}]_{>91\mathrm{d}}/\partial p$ (figure not shown), is also consistent with a smaller contribution of $-\partial\{[\overline{u}]_{>91\mathrm{d}}[\overline{\omega}]_{21-90\mathrm{d}}\}/\partial p$ to the total large-scale momentum tendency, particularly in the low to midtroposphere between 700 and 300 hPa over the WP, as shown in Fig. 9b.

d. Leading EOF mode of vertical subgrid-scale CMT profile and its modulation by the MJO

In this subsection, vertical profiles of subgrid-scale momentum tendency associated with the MJO are further examined from a different viewpoint. First, we carry out an EOF analysis of vertical momentum tendency profiles over the IO and WP to identify the leading mode of vertical tendency profiles based on the raw 6-hourly subgrid-scale tendency output from the CFSR. Preference of the leading momentum tendency mode relative to a particular MJO phase is then examined by conducting composite analysis of the principal component (PC) coefficients as a function of MJO phase.

To be consistent with momentum tendency profiles previously discussed based on a regression approach, two small equatorial regions are selected for the EOF analyses: one over the IO (1°S–1°N, 79°–81°E) and another over the WP (1°S–1°N, 154°–155°E). Similar

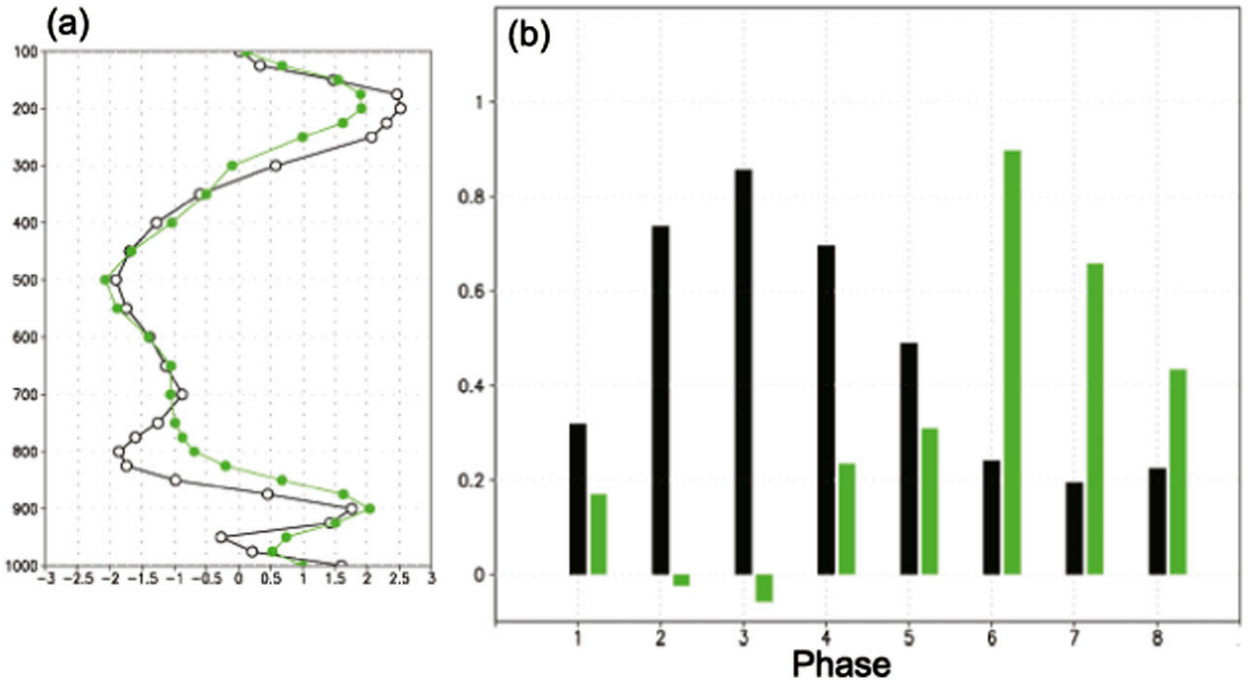

FIG. 11. (a) Vertical profiles of the first leading EOF mode of subgrid-scale momentum tendency over the IO (black) and WP (green). (b) Corresponding composite PC coefficients as a function of the RMM phases.

results can be obtained when different locations over the IO or WP are selected for the EOF analysis. The 6-hourly vertical profiles (37 levels) of subgrid-scale momentum tendency over these two selected spots during winters from 1998 to 2010 are obtained based on the raw 50-km CFSR output by averaging over these two boxes and then are subject to the EOF analysis. The first leading mode of vertical subgrid-scale momentum tendency, which is shown in Fig. 11, accounts for 32% and 31% of total variances over the IO and WP, respectively. Of particular interest, a three-layer structure in the vertical momentum tendency profile as previously described (i.e., a positive sign below 850 hPa, a negative sign between 850 and 300 hPa, and a positive sign above 300 hPa) is again discerned in the first leading modes over both the IO and WP (Fig. 11a), exhibiting great resemblances to the vertical profiles of regressed subgrid-scale momentum tendency pattern associated with the MJO, as shown in Fig. 2. Further composites of coefficients of the first leading PCs over both the IO and WP suggests that occurrence of the first leading subgrid-scale momentum tendency modes is greatly favored during the MJO peak phases (Fig. 11b). For example, the leading vertical momentum tendency mode over the IO is most favored during the MJO phase 3, when the active MJO convection is located over the eastern IO, while the leading subgrid-scale momentum tendency mode over the WP becomes most active during MJO phase 6, when local MJO convection reaches its maximum. The presence of positive composite PCs during the entire MJO cycle over the IO suggests prevalence of the three-layer subgrid-scale CMT profile on the seasonal mean time scale; while over the WP, the CMT tends to be more strongly controlled by the MJO. This intimate association between the preferred vertical three-layer subgrid-scale momentum tendency profile and MJO peak phases may suggest a two-way interaction between the MJO large-scale circulation and small-scale convection through momentum transport, as demonstrated by the idealized model in Majda and Stechmann (2009).

Since subgrid-scale momentum tendency from a model parameterization scheme only considers conditions on a local grid point, including cumulus mass fluxes and vertical wind profile, representation of impacts from organized MCSs has been a longstanding challenge for current weather and climate models (Tao and Moncrieff 2009; Moncrieff 2010). This model deficiency in resolving the MCSs justifies a mesoscale parameterization approach, for example, by estimating mesoscale momentum transport by using an archetypical dynamical model (Moncrieff 1992). Thus, it could be interesting to examine the mesoscale circulations associated with the first leading subgrid-scale momentum tendency mode based on the CFSR. Figure 12 illustrates regressed patterns of mesoscale circulation by the spatial filtering approach (u' and $-\omega'$; vectors) and vertical flux of zonal

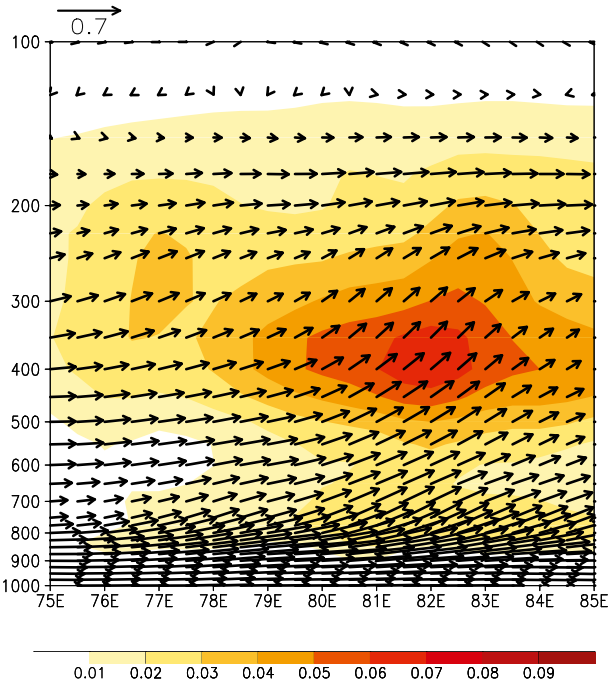

FIG. 12. Pressure–lon plots of the subgrid-scale CMT $-u'\omega'$ (shaded) and circulation [horizontal for zonal wind u' ($\mathrm{m\,s^{-1}}$) and vertical for pressure velocity ω' ($\mathrm{Pa\,s^{-1}}$ multiplied by a factor of -10); vectors] derived by regression onto the PC time series of the first leading EOF of the subgrid-scale momentum tendency over the IO.

momentum ($u'w'$; shading) against the PC time series of the first EOF mode of subgrid-scale momentum tendency over the IO. Interestingly, associated with the subgrid-scale momentum tendency over the small box over the IO, a well-organized relatively large-scale circulation is evident in the regression pattern with eastward tilting with height. This vertical tilting in circulation and associated vertical u-momentum transport greatly resembles the widely reported vertical structure of the organized convective systems and their impacts on environmental flow (Moncrieff 1992; LeMone and Moncrieff 1994; Mapes et al. 2006). As previously discussed, the mesoscale circulation derived based on the CFSR by the spatial filtering approach used in this study likely only marginally captures the observed mesoscale system because of the coarse spatial and temporal resolutions of the reanalysis dataset. Nevertheless, results in this part indicate that, although the subgrid-scale CMT is calculated independently on each model grid, to some extent, it may still be able to represent collective impacts from large-scale organized convection.

4. Summary and conclusions

While the prominent role of the Madden–Julian oscillation (MJO) in global climate and weather systems has been fully recognized, skillful simulation and prediction of the MJO still represent great challenges for current climate models, due largely to our insufficient understanding of the multiscale interactions associated with organized convection. In addition to exchanges of thermodynamical properties between multiscale convective systems and the MJO, which have been the main focus of previous studies, recent evidence based on limited observations, idealized model studies, and full-GCM simulations, indicate that momentum transport by organized convection could also play a crucial role in sustaining the MJO circulation. By capitalizing on the new-generation high-resolution reanalysis datasets with a long record, particularly on subgrid-scale convective momentum transport (CMT) fields archived from the CFSR and explicit momentum transport, we have comprehensively examined the structure of momentum tendency associated with the MJO at different spatial and temporal scales, with particular attention to the vertical transport of u momentum.

A three-layer vertical structure, as previously suggested in the mesoscale momentum tendency pattern associated with the MJO over the WP based on global CRM simulations, is also evident in the subgrid-scale CMT generated by the cumulus parameterization scheme in the CFSR model. In association with enhanced MJO convection over both the IO and WP, within and to the west of the MJO convection, positive, negative, and positive subgrid-scale momentum tendency anomalies are evident in the upper (300–100 hPa), middle (800–300 hPa), and lower (below 800 hPa) troposphere, respectively. A similar three-layer vertical subgrid-scale momentum tendency profile, but with an opposite sign, is observed to the east of the MJO convection. This subgrid-scale CMT vertical structure, on the one hand, tends to damp the large-scale MJO circulation in the free atmosphere above 800 hPa but enhances MJO winds in a shallow near-surface layer below 800 hPa. On the other hand, a tendency in generating a secondary circulation by this three-layer subgrid-scale profile near the MJO convection center could retard the eastward propagation of the MJO in the free atmosphere, while promoting the eastward propagation near the surface. As a result, the total momentum tendency could be partially responsible for the backward tilt with height in the observed MJO structure.

Further analyses based on the 50-km CFSR illustrate that u-momentum transport associated with the MJO by grid-scale circulation exhibits a similar three-layer vertical structure and comparable amplitude as the subgrid-scale CMT, but with an opposite sign. Total grid-scale CMT is further decomposed into a mesoscale and a remaining large-scale component following a spatial scale-separation approach with a cutoff scale of 5° radius for the

mesoscale system. As expected, the mesoscale CMT has a very weak amplitude because of the 50-km horizontal resolution of the CFSR data, and the total grid-scale momentum tendency is predominantly contributed by the large-scale circulation transport. It is noteworthy that, in spite of its weak amplitude, the vertical structure in mesoscale CMT associated with the MJO greatly resembles the subgrid-scale CMT and is in agreement with that by the 7-km CRM simulations in Miyakawa et al. (2012). This suggests that, although CMT by mesoscale systems cannot be fully resolved in the CFSR data at a 50-km resolution, the subgrid-scale CMT from the cumulus parameterization scheme may at least partly represent mesoscale CMT impacts as depicted in the previous CRM study. This notion is further supported by the well-organized vertically tilted mesoscale circulation obtained by regressing mesoscale-filtered momentum tendency fields against an index corresponding to the leading EOF mode of the subgrid-scale momentum tendency, as shown in section 3d.

It is further suggested that vertical u-momentum transport by large-scale circulation is mainly ascribed to transport of seasonal mean u by the MJO time-scale vertical motion. Vertical u-momentum transport by synoptic time-scale waves, which has been proposed to play a critical role for the MJO in recent idealized model studies, however, does not significantly contribute to the total grid-scale CMT, according to the analyses in this study based on the CFSR.

One of the main findings from this study is that the subgrid-scale CMT by the model parameterization (which could include mesoscale CMT in reality) could play an important role for the u-momentum budget associated with the MJO by largely offsetting the vertical grid-scale momentum transport induced by the MJO circulation itself. Therefore, if CMT impacts by small-scale convective systems are not properly represented in a GCM, the grid-scale momentum transport needs to be balanced by other terms; it thus could lead to model biases in simulating the MJO circulation. Cancellation between the subgrid- and grid-scale momentum tendencies was also noted in CRM simulations by Mapes and Wu (2001) and in global weather forecasts by the ECMWF model (MK97, their Fig. 8). This is likely because CMT processes are strong functions of the environmental vertical shear. For subgrid-scale momentum tendency, this involves compensating downwelling associated with the convective updraft [see the first term on the right-hand side of Eq. (1)], while for the grid-scale tendency, the transport is accomplished by the tilted organized circulations.

One caveat of this study is that subgrid-scale CMT output from the CFSR is sensitive to the parameterization scheme. Also, because of limitation in the horizontal resolution, the CMT impact on the MJO as a result of mesoscale systems cannot be well resolved in the CFSR model. To provide an independent validation of the results derived from CFSR, vertical CMT profiles associated with the MJO by subgrid-, meso-, and large-scale processes are also analyzed by using the EC–YOTC reanalysis during the period of two years. Largely similar results in CMT structure by the different spatial–temporal scales as those based on the CFSR are also evident in the analyses based on the EC–YOTC dataset. This further lends confidence to the findings derived in this study based on the CFSR.

Our results from the reanalyses, already noted as consistent with Miyakawa et al. (2012), are also consistent with the MK97 study of large-scale convective organization in the context of MJO observed during TOGA COARE and simulated by the ECMWF model on an 80-km grid. Specifically, they found that the subgrid-scale momentum tendency was dominated by, and had an opposite sign from, the meso- to large-scale momentum tendency associated with super clusters. The momentum tendency was approximated using the Moncrieff (1992) archetypal dynamical model of organized convection in sheared environments that represents upscale transport relevant to the organized deep convection phase of the MJO and the associated westerly wind bursts.

While results in this study as well as other previous observational and modeling studies suggest that the subgrid-scale CMT could play an important role for the observed MJO, it may not be the primary factor responsible for realistic representation of the MJO in a GCM. For example, even without including subgrid-scale CMT impacts on the large-scale flow, a superparameterized GCM, in which a 2D CRM is embedded within each grid box of the host model to replace the conventional cumulus parameterizations (Randall et al. 2003), can still largely capture the most important features of the observed MJO (e.g., Benedict and Randall 2009; Pritchard and Bretherton 2014). However, grid-scale momentum transport is likely to occur in superparameterized GCMs as an aliased form of subgrid CMT because differential latent heating by the CRMs in contiguous climate grids can generate horizontal pressure gradients. Moreover, deficiencies were also noted in these superparameterized GCM experiments [e.g., an overestimate of the intraseasonal convective activity over the WP (Benedict and Randall 2009)], which are likely because of unrealistic boundary layer interactions, a lack of weakening of the simulated disturbance over the Maritime Continent, and mean state differences (Benedict and Randall 2009). Additionally, based on a recent

global MJO model intercomparison project (Jiang et al. 2015), the two versions of superparameterized GCMs, one with atmosphere-only run, and another with atmosphere–ocean coupling, actually were not the top models in simulating the MJO among the total 27 models that participated in this project. Both of the two superparameterized model experiments exhibit large room for improvement in simulating the MJO. Therefore, missing processes in describing the subgrid-scale CMT feedbacks in these superparameterized GCM experiments could be partly responsible for the above model deficiencies.

Future studies warrant further investigations of the relative roles of different spatial–temporal scale systems for the total momentum transport associated with the MJO based on CRM simulations with a long record. A particular advantage of the CRM is the more complete resolution of mesoscale convective systems. Definitive observations are also needed to quantify important scale-dependent aspects and to evaluate CRM results. The most recent observations available from the Dynamics of the Madden–Julian Oscillation (DYNAMO; Yoneyama et al. 2013) field campaign may provide new insights into the role of the convective momentum transport associated with the MJO.

Acknowledgments. We thank anonymous reviewers for their critical comments on an earlier version of this paper. This work has greatly benefited from stimulating discussions with Drs. A. Majda, T. Miyakawa, B. Mapes, M. Zhao, and G. Zhang, and helpful comments from Drs. J. Stachnik, J. Han, and T. Kubar. We acknowledge support by the NSF Climate and Large-Scale Dynamics Program under Awards AGS-1228302 (XJ), AGS-1221013 (DW), and AGS-1360237 (RJ), and the NOAA MAPP Program under Award NA12OAR4310075 (XJ). Part of this research was carried out at the Jet Propulsion Laboratory, California Institute of Technology, under a contract with the National Aeronautics and Space Administration.

REFERENCES

Ajayamohan, R. S., B. Khouider, and A. J. Majda, 2013: Realistic initiation and dynamics of the Madden–Julian oscillation in a coarse resolution aquaplanet GCM. *Geophys. Res. Lett.,* **40,** 6252–6257, doi:10.1002/2013GL058187.

Arakawa, A., and W. H. Schubert, 1974: Interaction of a cumulus cloud ensemble with large-scale environment. Part I. *J. Atmos. Sci.,* **31,** 674–701, doi:10.1175/1520-0469(1974)031<0674:IOACCE>2.0.CO;2.

Benedict, J. J., and D. A. Randall, 2009: Structure of the Madden–Julian oscillation in the superparameterized CAM. *J. Atmos. Sci.,* **66,** 3277–3296, doi:10.1175/2009JAS3030.1.

Carr, M. T., and C. S. Bretherton, 2001: Convective momentum transport over the tropical Pacific: Budget estimates. *J. Atmos. Sci.,* **58,** 1673–1693, doi:10.1175/1520-0469(2001)058<1673:CMTOTT>2.0.CO;2.

Chen, S. S., R. A. Houze, and B. E. Mapes, 1996: Multiscale variability of deep convection in relation to large-scale circulation in TOGA COARE. *J. Atmos. Sci.,* **53,** 1380–1409, doi:10.1175/1520-0469(1996)053<1380:MVODCI>2.0.CO;2.

Del Genio, A. D., Y. Chen, D. Kim, and M.-S. Yao, 2012: The MJO transition from shallow to deep convection in *CloudSat*/*CALIPSO* data and GISS GCM simulations. *J. Climate,* **25,** 3755–3770, doi:10.1175/JCLI-D-11-00384.1.

Deng, L., and X. Wu, 2010: Effects of convective processes on GCM simulations of the Madden–Julian oscillation. *J. Climate,* **23,** 352–377, doi:10.1175/2009JCLI3114.1.

Duchon, C. E., 1979: Lanczos filtering in one and two dimensions. *J. Appl. Meteor.,* **18,** 1016–1022, doi:10.1175/1520-0450(1979)018<1016:LFIOAT>2.0.CO;2.

Han, Y., and B. Khouider, 2010: Convectively coupled waves in a sheared environment. *J. Atmos. Sci.,* **67,** 2913–2942, doi:10.1175/2010JAS3335.1.

Houze, R. A., 1973: Climatological study of vertical transports by cumulus-scale convection. *J. Atmos. Sci.,* **30,** 1112–1123, doi:10.1175/1520-0469(1973)030<1112:ACSOVT>2.0.CO;2.

——, 2004: Mesoscale convective systems. *Rev. Geophys.,* **42,** RG4003, doi:10.1029/2004RG000150.

——, S. S. Chen, D. E. Kingsmill, Y. Serra, and S. E. Yuter, 2000: Convection over the Pacific warm pool in relation to the atmospheric Kelvin–Rossby wave. *J. Atmos. Sci.,* **57,** 3058–3089, doi:10.1175/1520-0469(2000)057<3058:COTPWP>2.0.CO;2.

Huffman, G. J., R. F. Adler, B. Rudolf, U. Schneider, and P. R. Keehn, 1995: Global precipitation estimates based on a technique for combining satellite-based estimates, rain-gauge analysis, and NWP model precipitation information. *J. Climate,* **8,** 1284–1295, doi:10.1175/1520-0442(1995)008<1284:GPEBOA>2.0.CO;2.

Hung, M.-P., J.-L. Lin, W. Wang, D. Kim, T. Shinoda, and S. J. Weaver, 2013: MJO and convectively coupled equatorial waves simulated by CMIP5 climate models. *J. Climate,* **26,** 6185–6214, doi:10.1175/JCLI-D-12-00541.1.

Jiang, X., D. Waliser, J.-L. Li, and C. Woods, 2011: Vertical cloud structures of the boreal summer intraseasonal variability based on *CloudSat* observations and ERA-Interim reanalysis. *Climate Dyn.,* **36,** 2219–2232, doi:10.1007/s00382-010-0853-8.

——, and Coauthors, 2015: Vertical structure and physical processes of the Madden–Julian oscillation: Exploring key model physics in climate simulations. *J. Geophys. Res. Atmos.,* doi:10.1002/2014JD022375, in press.

Johnson, R. H., T. M. Rickenbach, S. A. Rutledge, P. E. Ciesielski, and W. H. Schubert, 1999: Trimodal characteristics of tropical convection. *J. Climate,* **12,** 2397–2418, doi:10.1175/1520-0442(1999)012<2397:TCOTC>2.0.CO;2.

Khouider, B., 2006: A simple multicloud parameterization for convectively coupled tropical waves. Part I: Linear analysis. *J. Atmos. Sci.,* **63,** 1308–1323, doi:10.1175/JAS3677.1.

——, 2007: A simple multicloud parameterization for convectively coupled tropical waves. Part II: Nonlinear simulations. *J. Atmos. Sci.,* **64,** 381–400, doi:10.1175/JAS3833.1.

——, and A. J. Majda, 2006: Model multi-cloud parameterizations for convectively coupled waves: Detailed nonlinear wave evolution. *Dyn. Atmos. Oceans,* **42,** 59–80, doi:10.1016/j.dynatmoce.2005.12.001.

——, and ——, 2008a: Multicloud models for organized tropical convection: Enhanced congestus heating. *J. Atmos. Sci.,* **65,** 895–914, doi:10.1175/2007JAS2408.1.

——, and ——, 2008b: Equatorial convectively coupled waves in a simple multicloud model. *J. Atmos. Sci.,* **65,** 3376–3397, doi:10.1175/2008JAS2752.1.

——, A. St-Cyr, A. J. Majda, and J. Tribbia, 2011: The MJO and convectively coupled waves in a coarse-resolution GCM with a simple multicloud parameterization. *J. Atmos. Sci.,* **68,** 240–264, doi:10.1175/2010JAS3443.1.

——, Y. Han, and J. A. Biello, 2012a: Convective momentum transport in a simple multicloud model for organized convection. *J. Atmos. Sci.,* **69,** 281–302, doi:10.1175/JAS-D-11-042.1.

——, ——, A. J. Majda, and S. N. Stechmann, 2012b: Multiscale waves in an MJO background and convective momentum transport feedback. *J. Atmos. Sci.,* **69,** 915–933, doi:10.1175/JAS-D-11-0152.1.

Kikuchi, K., and Y. N. Takayabu, 2004: The development of organized convection associated with the MJO during TOGA COARE IOP: Trimodal characteristics. *Geophys. Res. Lett.,* **31,** L10101, doi:10.1029/2004GL019601.

——, and B. Wang, 2010: Spatiotemporal wavelet transform and the multiscale behavior of the Madden–Julian oscillation. *J. Climate,* **23,** 3814–3834, doi:10.1175/2010JCLI2693.1.

Kiladis, G. N., M. C. Wheeler, P. T. Haertel, K. H. Straub, and P. E. Roundy, 2009: Convectively coupled equatorial waves. *Rev. Geophys.,* **47,** RG2003, doi:10.1029/2008RG000266.

Kim, D., J.-S. Kug, I.-S. Kang, F.-F. Jin, and A. T. Wittenberg, 2008: Tropical Pacific impacts of convective momentum transport in the SNU coupled GCM. *Climate Dyn.,* **31,** 213–226, doi:10.1007/s00382-007-0348-4.

——, and Coauthors, 2009: Application of MJO simulation diagnostics to climate models. *J. Climate,* **22,** 6413–6436, doi:10.1175/2009JCLI3063.1.

Kiranmayi, L., and E. D. Maloney, 2011: Intraseasonal moist static energy budget in reanalysis data. *J. Geophys. Res.,* **116,** D21117, doi:10.1029/2011JD016031.

Lau, W. K.-M., and D. E. Waliser, 2012: *Intraseasonal Variability in the Atmosphere–Ocean Climate System.* 2nd ed. Springer, 613 pp.

LeMone, M. A., and M. W. Moncrieff, 1994: Momentum and mass transport by convective bands: Comparisons of highly idealized dynamical models to observations. *J. Atmos. Sci.,* **51,** 281–305, doi:10.1175/1520-0469(1994)051<0281:MAMTBC>2.0.CO;2.

Lin, J. L., M. H. Zhang, and B. Mapes, 2005: Zonal momentum budget of the Madden–Julian oscillation: The source and strength of equivalent linear damping. *J. Atmos. Sci.,* **62,** 2172–2188, doi:10.1175/JAS3471.1.

Lin, J.-L., and Coauthors, 2006: Tropical intraseasonal variability in 14 IPCC AR4 climate models. Part I: Convective signals. *J. Climate,* **19,** 2665–2690, doi:10.1175/JCLI3735.1.

Lin, J. L., B. E. Mapes, and W. Q. Han, 2008: What are the sources of mechanical damping in Matsuno–Gill-type models? *J. Climate,* **21,** 165–179, doi:10.1175/2007JCLI1546.1.

Lin, X., and R. H. Johnson, 1996: Heating, moistening, and rainfall over the western Pacific warm pool during TOGA COARE. *J. Atmos. Sci.,* **53,** 3367–3383, doi:10.1175/1520-0469(1996)053<3367:HMAROT>2.0.CO;2.

Madden, R. A., and P. R. Julian, 1971: Detection of a 40–50 day oscillation in zonal wind in the tropical Pacific. *J. Atmos. Sci.,* **28,** 702–708, doi:10.1175/1520-0469(1971)028<0702:DOADOI>2.0.CO;2.

——, and ——, 1994: Observations of the 40–50-day tropical oscillation: A review. *Mon. Wea. Rev.,* **122,** 814–837, doi:10.1175/1520-0493(1994)122<0814:OOTDTO>2.0.CO;2.

Majda, A. J., 2007: New multiscale models and self-similarity in tropical convection. *J. Atmos. Sci.,* **64,** 1393–1404, doi:10.1175/JAS3880.1.

——, and J. A. Biello, 2004: A multiscale model for tropical intraseasonal oscillations. *Proc. Natl. Acad. Sci. USA,* **101,** 4736–4741, doi:10.1073/pnas.0401034101.

——, and S. N. Stechmann, 2008: Stochastic models for convective momentum transport. *Proc. Natl. Acad. Sci. USA,* **105,** 17 614–17 619, doi:10.1073/pnas.0806838105.

——, and ——, 2009: A simple dynamical model with features of convective momentum transport. *J. Atmos. Sci.,* **66,** 373–392, doi:10.1175/2008JAS2805.1.

——, and ——, 2011: Multiscale theories for the MJO. *Intraseasonal Variability in the Atmosphere–Ocean Climate System,* 2nd ed. W. K.-M. Lau and D. E. Waliser, Eds., Springer, 549–564.

——, and ——, 2015: Models for multiscale interactions. II: Madden–Julian oscillation, moisture, and convective momentum transport. *Multiscale Convection-Coupled Systems in the Tropics: A Tribute to Michio Yanai,* Meteor. Monogr., Amer. Meteor. Soc., in press.

Mapes, B. E., and J. T. Bacmeister, 2012: Diagnosis of tropical biases and the MJO from patterns in the MERRA analysis tendency fields. *J. Climate,* **25,** 6202–6214, doi:10.1175/JCLI-D-11-00424.1.

——, and X. Wu, 2001: Convective eddy momentum tendencies in long cloud-resolving model simulations. *J. Atmos. Sci.,* **58,** 517–526, doi:10.1175/1520-0469(2001)058<0517:NACCEM>2.0.CO;2.

——, S. Tulich, J. Lin, and P. Zuidema, 2006: The mesoscale convection life cycle: Building block or prototype for large-scale tropical waves? *Dyn. Atmos. Oceans,* **42,** 3–29, doi:10.1016/j.dynatmoce.2006.03.003.

Miura, H., M. Satoh, T. Nasuno, A. T. Noda, and K. Oouchi, 2007: A Madden–Julian oscillation event realistically simulated by a global cloud-resolving model. *Science,* **318,** 1763–1765, doi:10.1126/science.1148443.

Miyakawa, T., Y. N. Takayabu, T. Nasuno, H. Miura, M. Satoh, and M. W. Moncrieff, 2012: Convective momentum transport by rainbands within a Madden–Julian oscillation in a global nonhydrostatic model with explicit deep convective processes. Part I: Methodology and general results. *J. Atmos. Sci.,* **69,** 1317–1338, doi:10.1175/JAS-D-11-024.1.

Moncrieff, M. W., 1992: Organized convective systems: Archetypal dynamic models, mass and momentum flux theory, and parametrization. *Quart. J. Roy. Meteor. Soc.,* **118,** 819–850, doi:10.1002/qj.49711850703.

——, 2010: The multiscale organization of moist convection and the intersection of weather and climate. *Climate Dynamics: Why Does Climate Vary? Geophys. Monogr.,* Vol. 189, Amer. Geophys. Union, 3–26.

——, and E. Klinker, 1997: Organized convective systems in the tropical western Pacific as a process in general circulation models: A TOGA COARE case-study. *Quart. J. Roy. Meteor. Soc.,* **123,** 805–827, doi:10.1002/qj.49712354002.

——, D. E. Waliser, M. J. Miller, M. A. Shapiro, G. R. Asrar, and J. Caughey, 2012: Multiscale convective organization and the YOTC virtual global field campaign. *Bull. Amer. Meteor. Soc.,* **93,** 1171–1187, doi:10.1175/BAMS-D-11-00233.1.

Moorthi, S., H.-L. Pan, and P. Caplan, 2001: Changes to the 2001 NCEP operational MRF/AVN global analysis/forecast system. National Weather Service Tech. Procedures Bull. 484, 14 pp. [Available online at http://www.nws.noaa.gov/om/tpb/484.pdf.]

Nakazawa, T., 1988: Tropical super clusters within intraseasonal variations over the western Pacific. *J. Meteor. Soc. Japan,* **66,** 823–839.

Neelin, J. D., and I. M. Held, 1987: Modeling tropical convergence based on the moist static energy budget. *Mon. Wea. Rev.,* **115,** 3–12, doi:10.1175/1520-0493(1987)115<0003:MTCBOT>2.0.CO;2.

Pan, H., and W. Wu, 1995: Implementing a mass flux convective parameterization package for the NMC medium-range forecast model. National Meteorological Center Office Note 409, 40 pp. [Available online at http://www.lib.ncep.noaa.gov/ncepofficenotes/files/01408A42.pdf.]

Pritchard, M. S., and C. S. Bretherton, 2014: Causal evidence that rotational moisture advection is critical to the superparameterized Madden–Julian oscillation. *J. Atmos. Sci.,* **71,** 800–815, doi:10.1175/JAS-D-13-0119.1.

Randall, D., M. Khairoutdinov, A. Arakawa, and W. Grabowski, 2003: Breaking the cloud parameterization deadlock. *Bull. Amer. Meteor. Soc.,* **84,** 1547–1564, doi:10.1175/BAMS-84-11-1547.

Rauniyar, S. P., and K. J. E. Walsh, 2011: Scale interaction of the diurnal cycle of rainfall over the Maritime Continent and Australia: Influence of the MJO. *J. Climate,* **24,** 325–348, doi:10.1175/2010JCLI3673.1.

Raymond, D. J., S. Sessions, A. Sobel, and Z. Fuchs, 2009: The mechanics of gross moist stability. *J. Adv. Model. Earth Syst.,* **1** (3), 9, doi:10.3894/james.2009.1.9.

Richter, J. H., and P. J. Rasch, 2008: Effects of convective momentum transport on the atmospheric circulation in the Community Atmosphere Model, version 3. *J. Climate,* **21,** 1487–1499, doi:10.1175/2007JCLI1789.1.

Roundy, P. E., 2008: Analysis of convectively coupled Kelvin waves in the Indian Ocean MJO. *J. Atmos. Sci.,* **65,** 1342–1359, doi:10.1175/2007JAS2345.1.

Saha, S., and Coauthors, 2010: The NCEP Climate Forecast System Reanalysis. *Bull. Amer. Meteor. Soc.,* **91,** 1015–1057, doi:10.1175/2010BAMS3001.1.

Satoh, M., T. Matsuno, H. Tomita, H. Miura, T. Nasuno, and S. Iga, 2008: Nonhydrostatic icosahedral atmospheric model (NICAM) for global cloud resolving simulations. *J. Comput. Phys.,* **227,** 3486–3514, doi:10.1016/j.jcp.2007.02.006.

Schumacher, C., and R. A. Houze, 2003: Stratiform rain in the tropics as seen by the TRMM precipitation radar. *J. Climate,* **16,** 1739–1756, doi:10.1175/1520-0442(2003)016<1739:SRITTA>2.0.CO;2.

Shapiro, L. J., and D. E. Stevens, 1980: Parameterization of convective effects on the momentum and vorticity budgets of synoptic-scale Atlantic tropical waves. *Mon. Wea. Rev.,* **108,** 1816–1826, doi:10.1175/1520-0493(1980)108<1816:POCEOT>2.0.CO;2.

Sherwood, S. C., 1999: Convective precursors and predictability in the tropical western Pacific. *Mon. Wea. Rev.,* **127,** 2977–2991, doi:10.1175/1520-0493(1999)127<2977:CPAPIT>2.0.CO;2.

Slingo, J. M., and Coauthors, 1996: Intraseasonal oscillations in 15 atmospheric general circulation models: Results from an AMIP diagnostic subproject. *Climate Dyn.,* **12,** 325–357, doi:10.1007/BF00231106.

Song, X., X. Wu, G. J. Zhang, and R. W. Arritt, 2008: Understanding the effects of convective momentum transport on climate simulations: The role of convective heating. *J. Climate,* **21,** 5034–5047, doi:10.1175/2008JCLI2187.1.

Takaya, K., and H. Nakamura, 2001: A formulation of a phase-independent wave-activity flux for stationary and migratory quasigeostrophic eddies on a zonally varying basic flow. *J. Atmos. Sci.,* **58,** 608–627, doi:10.1175/1520-0469(2001)058<0608:AFOAPI>2.0.CO;2.

Takayabu, Y. N., 1994: Large-scale cloud disturbances associated with equatorial waves. Part I. Spectral features of the cloud disturbances. *J. Meteor. Soc. Japan,* **72,** 433–449.

——, and M. Murakami, 1991: The structure of super cloud clusters observed in 1–20 June 1986 and their relationship to easterly waves. *J. Meteor. Soc. Japan,* **69,** 105–125.

——, K. M. Lau, and C. H. Sui, 1996: Observation of a quasi-2-day wave during TOGA COARE. *Mon. Wea. Rev.,* **124,** 1892–1913, doi:10.1175/1520-0493(1996)124<1892:OOAQDW>2.0.CO;2.

Tao, W. K., and M. W. Moncrieff, 2009: Multiscale cloud system modeling. *Rev. Geophys.,* **47,** RG4002, doi:10.1029/2008RG000276.

Tung, W. W., and M. Yanai, 2002a: Convective momentum transport observed during the TOGA COARE IOP. Part I: General features. *J. Atmos. Sci.,* **59,** 1857–1871, doi:10.1175/1520-0469(2002)059<1857:CMTODT>2.0.CO;2.

——, and ——, 2002b: Convective momentum transport observed during the TOGA COARE IOP. Part II: Case studies. *J. Atmos. Sci.,* **59,** 2535–2549, doi:10.1175/1520-0469(2002)059<2535:CMTODT>2.0.CO;2.

Waliser, D. E., and Coauthors, 2012: The ''Year'' of Tropical Convection (May 2008–April 2010): Climate variability and weather highlights. *Bull. Amer. Meteor. Soc.,* **93,** 1189–1218, doi:10.1175/2011BAMS3095.1.

Wang, B., and T. M. Li, 1994: Convective interaction with boundary-layer dynamics in the development of a tropical intraseasonal system. *J. Atmos. Sci.,* **51,** 1386–1400, doi:10.1175/1520-0469(1994)051<1386:CIWBLD>2.0.CO;2.

——, and F. Liu, 2011: A model for scale interaction in the Madden–Julian oscillation. *J. Atmos. Sci.,* **68,** 2524–2536, doi:10.1175/2011JAS3660.1.

Webster, P. J., and R. Lukas, 1992: TOGA COARE—The Coupled Ocean Atmosphere Response Experiment. *Bull. Amer. Meteor. Soc.,* **73,** 1377–1416, doi:10.1175/1520-0477(1992)073<1377:TCTCOR>2.0.CO;2.

Wheeler, M. C., and H. H. Hendon, 2004: An all-season real-time multivariate MJO index: Development of an index for monitoring and prediction. *Mon. Wea. Rev.,* **132,** 1917–1932, doi:10.1175/1520-0493(2004)132<1917:AARMMI>2.0.CO;2.

Wu, X., L. Deng, X. Song, G. Vettoretti, W. R. Peltier, and G. J. Zhang, 2007: Impact of a modified convective scheme on the Madden–Julian oscillation and El Niño–Southern Oscillation in a coupled climate model. *Geophys. Res. Lett.,* **34,** L16823, doi:10.1029/2007GL030637.

Yang, G. Y., and J. Slingo, 2001: The diurnal cycle in the tropics. *Mon. Wea. Rev.,* **129,** 784–801, doi:10.1175/1520-0493(2001)129<0784:TDCITT>2.0.CO;2.

Yang, M. J., and R. A. Houze, 1996: Momentum budget of a squall line with trailing stratiform precipitation: Calculations with a high-resolution numerical model. *J. Atmos. Sci.,* **53,** 3629–3652, doi:10.1175/1520-0469(1996)053<3629:MBOASL>2.0.CO;2.

Yoneyama, K., C. Zhang, and C. N. Long, 2013: Tracking pulses of the Madden–Julian oscillation. *Bull. Amer. Meteor. Soc.,* **94,** 1871–1891, doi:10.1175/BAMS-D-12-00157.1.

Yuan, J., and R. A. Houze, 2010: Global variability of mesoscale convective system anvil structure from A-Train satellite data. *J. Climate,* **23,** 5864–5888, doi:10.1175/2010JCLI3671.1.

Zhang, C. D., 2005: Madden–Julian oscillation. *Rev. Geophys.,* **43,** RG2003, doi:10.1029/2004RG000158.

——, J. Gottschalck, E. D. Maloney, M. W. Moncrieff, F. Vitart, D. E. Waliser, B. Wang, and M. C. Wheeler, 2013: Cracking the MJO nut. *Geophys. Res. Lett.,* **40,** 1223–1230, doi:10.1002/grl.50244.

Zhou, L., R. B. Neale, M. Jochum, and R. Murtugudde, 2012: Improved Madden–Julian oscillations with improved physics: The impact of modified convection parameterizations. *J. Climate,* **25,** 1116–1136, doi:10.1175/2011JCLI4059.1.